Non-Newtonian ViRheometry via Similarity Analysis

MITSUKI HAMAMICHI, Aoyama Gakuin University (AGU), Japan
KENTARO NAGASAWA, The University of Tokyo, Japan
MASATO OKADA, The University of Tokyo, Japan
RYOHEI SETO, Wenzhou Institute, University of Chinese Academy of Sciences / Oujiang Laboratory, China
YONGHAO YUE, Aoyama Gakuin University (AGU), Japan

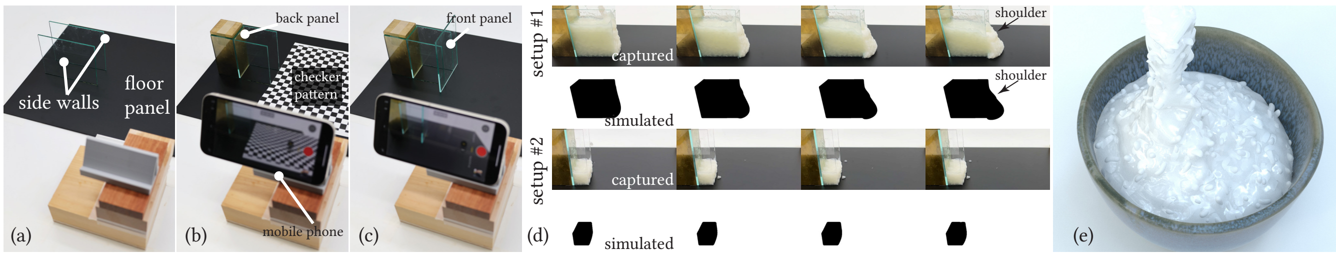

Fig. 1. We (a–c) configure dam-break setups and (d) perform experiments for real world fluid-like material and employ optimizations via simulations to estimate the Herschel–Bulkley material parameters. (e) The estimated parameters are ready for reproducing intriguing behaviors of real world materials.

We estimate the three Herschel–Bulkley parameters (yield stress σ_Y, power-law index n, and consistency parameter η) for shear-dependent fluid-like materials possibly with large-scale inclusions, for which rheometers may fail to provide a useful measurement. We perform experiments using the unknown material for dam-break (or column collapse) setups and capture video footage. We then use simulations to optimize for the material parameters. For better match up with the simple shear flow encountered in a rheometer, we modify the flow rule for the elasto-viscoplastic Herschel–Bulkley model. Analyzing the loss landscape for optimization, we realize a *similarity relation*; material parameters far away within this relation would result in matched simulations, making it hard to distinguish the parameters. We found that by exploiting the setup dependency of the similarity relation, we can improve on the estimation using multiple setups, which we propose by analyzing the Hessian of the similarity relation. We validate the efficacy of our method by comparing the estimations to the measurements from a rheometer (for materials without large-scale inclusions) and show applications to materials with large-scale inclusions, including various salad or pasta sauces, and congee.

CCS Concepts: • **Computing methodologies → Physical simulation**.

Additional Key Words and Phrases: Material parameter estimation, Herschel–Bulkley, shear thinning fluids, large-scale inclusions, video-based estimation

Authors' addresses: Mitsuki Hamamichi, Aoyama Gakuin University (AGU), Japan; Kentaro Nagasawa, The University of Tokyo, Japan; Masato Okada, The University of Tokyo, Kiban 701, Kashiwa-no-ha 5-1-5, Kashiwa-shi, Chiba, 277-8561, Japan; Ryohei Seto, Wenzhou Institute, University of Chinese Academy of Sciences / Oujiang Laboratory, Wenzhou, Zhejiang, 325000, China; Yonghao Yue, Aoyama Gakuin University (AGU), O-525, Fuchinobe 5-10-1, Chuo-ku, Sagamihara, Kanagawa, 252-5258, Japan, yonghao@it.aoyama.ac.jp.

0730-0301/2023/12-ART193
https://doi.org/10.1145/3618310

ACM Reference Format:
Mitsuki Hamamichi, Kentaro Nagasawa, Masato Okada, Ryohei Seto, and Yonghao Yue. 2023. Non-Newtonian ViRheometry via Similarity Analysis. *ACM Trans. Graph.* 42, 6, Article 193 (December 2023), 16 pages. https://doi.org/10.1145/3618310

1 INTRODUCTION

Fluid-like foods are common in our daily life, yet they span a wide material space: for example, water, orange juice, and comsommé are perhaps at the thin end, which flow smoothly; French dressing, syrup, and tartar sauce are viscous and stick to other foods, while mayo, mustard, guacamole, wasabi, and pâté are thicker and more like a solid. Sesame dressings, salsa sauce, and ragú sauce are mixtures of clearly visible solid inclusions and fluids.

Most of these fluid-like foods are *non-Newtonian*; they may have a yield stress so that they behave like an elastic solid under low applied forces and start to flow when the applied forces become large enough, as well as a shear-dependent viscosity so that the magnitude of the viscosity may increase (shear-thickening) or decrease (shear-thinning) as the applied forces are increased. These non-Newtonian properties are nature of complex fluids, giving them various functionalities that we make use of everyday: a food is easier to swallow if it is less viscous or shear-thinning (viscosity decreased when being swallowed); a pâté should stay in shape on a plate while flow easily when taken on a knife and smeared over a bread.

The widely varied material properties in fluids [Barnes 2000] are also common and utilized in industry, including cosmetics, pharmaceuticals, and lubricants. The acquisition of the material properties is important for maintaining stable product quality[1], designing new products with desired material properties, as well as for reproducing photo-realistic animations.

[1]For example, the production of ketchup in a stable quality needs to account for the variations in the material property of the tomato pastes due to cultivation and processing conditions [Bayod et al. 2008].

Despite the importance of material property acquisition, the technologies available nowadays are still not general enough for a variety of our daily materials. Aiming at accurate measurements, we have devices called *rheometers*, where the accuracy comes at the cost of applying a *well-controlled, idealized flow* to the specimen. To prevent (non-ideal) secondary flows, this usually means the specimen is put in a narrow gap, limiting the particle size of the specimen to be smaller than 5–20 μm [Whaley et al. 2019], excluding materials with *large (millimeter) scale inclusions*, like sesames in a dressing or diced pancetta in a pasta sauce. Recovering an ideal flow or performing post-process corrections requires material-dependent design of equipment or expert knowledge; there is no rheometer proved to work for a variety of large-scale inclusions to our knowledge. In addition, a rheometer is usually expensive (like 50k US dollars) and not easily available for daily use [Nagasawa et al. 2019]. On the other hand, recent development in *video-based estimation* techniques (together with optimization over simulations) aims at the easiness of use and allows for flows in the wild (as opposed to the idealized flows), but the easiness usually comes at the cost of a *simplified material model*, e.g., purely elastic [Wang et al. 2015] or purely Newtonian [Takahashi and Lin 2019].

Our work is on the line of the latter video-based estimation techniques, and we extend the work of Takahashi et al. [2019] to handle *non-Newtonian fluids* with possibly *stationary distributed large-scale inclusions*, meaning that the inclusions (if exist) are uniformly distributed so that the material as a whole can be viewed as a *homogeneous continuum* (e.g., congee and sesame dressings). This modeling assumption is useful for representing and simulating various fluid-like foods, including those seemingly inhomogeneous ones, listed at the beginning of this section, via a standard continuum mechanics approach (such as MPM [Stomakhin et al. 2013; Sulsky et al. 1994, 1995]) without effort for simulating each inclusion independently.

We estimate the constitutive model of the material flow, described by the relation (called *flow curve*) between the shear stress σ_s (the shear component of the Cauchy stress) and shear rate $\dot{\gamma}$: $\sigma_\mathrm{s} = f(\dot{\gamma})$. For many materials, including fluid-like foods [Nagasawa et al. 2019], water-clay mixtures [Maciel et al. 2009], debris flow [Coussot and Piau 1995; Pellegrino and Schippa 2018], and even fabric–water mixtures in washing machines [Loyola et al. 2018], to just list a few, the flow curves can be fitted by the Herschel–Bulkley model [Herschel and Bulkley 1926],

$$\sigma_\mathrm{s} = \eta\dot{\gamma}^n + \sigma_\mathrm{Y}, \tag{1}$$

where σ_Y is the yield stress, n is the power-law index, and η is the consistency parameter. The Herschel–Bulkley model encompasses several important classes: setting $n = 1$ recovers the Bingham model, setting $\sigma_\mathrm{Y} = 0$ recovers the power law model, and setting both $\sigma_\mathrm{Y} = 0$ and $n = 1$ recovers the Newtonian model. We estimate the three parameters η, n, and σ_Y of the Herschel–Bulkley constitutive relation (1), assuming those are independent of its flow history (or in other words, we assume the material is *non-thixotropic*). We limit the search scope of the parameters to the *material space* $\mathfrak{M} := \{10^{-4} \leq \eta/(\mathrm{Pa\,s}^n) \leq 30,\ 0.3 \leq n \leq 1.0,\ 0 \leq \sigma_\mathrm{Y}/(\mathrm{Pa}) \leq 40\}$[2]. We limit ourselves to *shear-thinning materials*, due to the limited availability of well-homogenized shear-thickening materials for testing. We assume that the bulk and shear moduli satisfy $\kappa \geq 10^4\,\mathrm{Pa}$ and $\mu \geq 10^3\,\mathrm{Pa}$, respectively. We do not estimate these elastic moduli nor require their precise values to be known *a priori*; our discussion (§ 4) and results (§ 7) show that we can still estimate the parameters η, n, and σ_Y (i.e., our method exclusively estimate the three parameters η, n, and σ_Y).

To simulate a Herschel–Bulkley material, we modify the elasto-viscoplastic Herschel–Bulkley model [Nagasawa et al. 2019; Yue et al. 2015] to better match the scalar constitutive relation (1) seen by a rheometer. We also give a comprehensive understanding between an elasto-viscoplastic Herschel–Bulkley model (i.e., a solid model) and a Herschel–Bulkley fluid model.

Unlike purely Newtonian fluids, where the fluid is solely characterized by a single viscosity parameter η, the multiple parameters and non-linearity in a Herschel–Bulkley material may result in different parameter sets to end up with an almost identical behavior for a given setup. This defines a *similarity relation* between fluids with different parameter sets, a concept analogous to the similarity relation in rendering for participating media [Zhao et al. 2014].

An interesting question is whether we can further pin down the material parameters by, e.g., making use of multiple videos taken for different setups, and if yes, how to appropriately choose such setups. Our answers to these questions are positive. We found that although it is hard to directly analyze the similarity relation for the *simulated* results, it is possible to analytically consider the similarity relation for the so-called *plane Poiseuille flow* [Poiseuille 1840] of a Herschel–Bulkley fluid, which allows for a *differential analysis* between different setups of the plane Poiseuille flow and the degrees of ambiguity in the Hershcel–Bulkley parameters. The insight from this differential analysis can be transferred to propose additional setups in the video-based rheometry (*ViRheometry*).

We use the dam-break (or column collapse) setups to perform experiments to allow for materials with *large-scale* inclusions, as well as for the easiness of preparing different setups by changing their width and height. We designed our setups using only off-the-shelf materials with minimum necessity on the control of the experiments, for the accessibility to non-expert (graphics) users. We use footage at the beginning of the flow in a short time window of 1/3 seconds (before the material spreads widely) to minimize the effect of surface tension, which we ignore in our simulation[3].

We validate the efficacy of our method by comparing the estimations to the measurements from a rotational rheometer (Figures 13 and 11) and show applications to materials possibly with large-scale inclusions, including various salad or pasta sauces, and congee (Figures 1 and 12).

2 RELATED WORK

2.1 Physical Measurements

There are a variety of methods (typically using a *rheometer*) for physical measurements of the flowing properties of the target material (see reviews by, e.g., Macosko [1994], Barnes [1989], Larson [1998],

[2]The search space is determined such that it covers a wide range of our daily materials (as we demonstrate in the paper), while excluding materials that do not flow with our experiment setups.

[3]We note that ignoring the surface tension can be problematic depending on the simulation scale.

Dogan and Kokini [2006], Mezger [2012], and Zheng [2019]). To analyze *viscoelastic* behaviors, one can perform *oscillatory tests*. An established class of such measurements is the small amplitude oscillatory shear (SAOS) (see the review by, e.g., Whaley et al. [2019]), which is limited to linear viscoelasticity, and hence not suitable for large shear deformation. Extensions to nonlinear viscoelasticity called large amplitude oscillatory shear (LAOS) (see the review by, e.g., Hyun et al. [2011]) have been actively researched, but a material-independent framework has not been established. A typical way to measure the response of a large shear flow is instead to perform *steady-shear tests*, which are designed to measure *multiple* flow conditions under different strain rates, necessary for non-Newtonian fluids to account for their *rate-dependency*.

In a steady shear test, the effective viscosities are assessed by putting the specimen in a *gap* realizing a *laminar* flow with a controllable strain rate, followed by measuring the required shear stress for achieving the flow. Such a laminar flow can be realized by drag flows (e.g., Couette type rotational rheometers [Couette 1890]) or pressure-driven flows (e.g., capillary (or pipe) rheometers initiated independently by Hagen [1839] and Poiseuille [1840]). For an accurate measurement, it is important 1) to avoid secondary flows or Taylor vortices for an ideal laminar flow, as well as 2) to reduce the material dependencies in the strain profile. If these conditions are met, the effective viscosities can be identified in *absolute* physical units, enabling *absolute measurements*, giving rise to the flow curves (relations between the stress and strain rate), which can be then fitted using prescribed constitutive models (e.g., the work of Mullineux [2008] and Magnon and Cayeux [2021]). For satisfying these conditions, the ideal apparatuses (e.g., for a cone-and-plate or parallel-plate rotational rheometer [Mooney and Ewart 1934]) come with a narrow gap (at the order of millimeter to a few centimeters), excluding materials with millimeter-scale large inclusions.

Although devices not fulfilling the above conditions (including many viscometers and rotational rheometers used with certain types of geometries, e.g., a wide gap) only return device-specific viscosity-related indices for non-Newtonian fluids, they are still useful for comparing the flowing behavior *relative* to a canonical reference, allowing for *relative measurements*. A popular example is the Bostwick consistometer (developed by E. P. Bostwick around 1938 [Eolkin 1957; Perona 2005]), a device much simpler and less expensive compared to rheometers. A Bostwick consistometer consists of a rectangular container with a gate to allow one to perform a simple dam-break test and measure the distance the specimen flows in a given time interval.

There are studies trying to understand the flow in a measurement device, via, e.g., theoretical analyses [Milczarek and McCarthy 2006], numerical simulations [Savarmand et al. 2007], or tomographic techniques [Choi et al. 2002; McCarthy and McCarthy 2009], to correlate the measurements with material parameters (e.g., for a power law [Milczarek and McCarthy 2006] or a Herschel–Bulkley model [Loyola et al. 2018; McCarthy and McCarthy 2009]), or to validate or build customized wide-gap rheometers (e.g., the work of Coussot and Piau [1995], Schatzmann et al. [2009], Heirman et al. [2008] and Loyola et al. [2018]). Like these work, assessments of the validity usually needs expert knowledge and/or the understanding of the flow *per setting*.

On the line of the research on the above assessments, Sao et al. [2021] proposed an apparatus that uses ultrasonic and laser sensors to measure the depth and velocity of a steady flow down a slope to estimate the Herschel–Bulkley parameters of the flow. Compared to their approach, our setting is much more conventional; we do not need to maintain a steady flow nor do we need the ultrasonic and laser sensors.

2.2 Video-Based Estimation

Video-based estimation aims at the acquisition of material properties by using usually simple, convenient, and inexpensive settings for possible complex material behaviors (e.g., inhomogeneous strain rates), typically in conjunction with accurate physical modeling of an *a priori* specified material model; this is in contrast to physical (absolute) measurements, where usually sophisticated settings are used to constrain a simple material behavior (e.g., a laminar flow), together with minimum assumptions on the material model. Such an estimation at a high level typically solves an *inverse problem* via *optimization*, a framework widely adopted in mechanical engineering for estimating material parameters for constitutive equations from observed quantities (e.g., the work of Mahnken [2004]), but methods in graphics focus more on non-ideal objects in the wild (e.g., complex shapes and/or material behaviors).

Previous methods in graphics have focused on, e.g., capturing rigid-body dynamics [Bhat et al. 2002], collisions [Monszpart et al. 2016], frictional contacts [Rasheed et al. 2021], elastic deformations [Bickel et al. 2009; Wang et al. 2015], and viscosities [Takahashi and Lin 2019]. We extended the method by Takahashi et al. [2019] for Newtonian fluids to non-Newtonian materials. Concurrent to our work, Zhang et al. [2023] proposed using a monocular video together with a setup injecting the specimen from a nozzle to estimate parameters for non-Newtonian materials. By using multiple dam-break setups in our method, we can alleviate inclusions getting clogged in the setup, as well as reduce the indeterminacy of the estimated parameters. Further, we provide validations (for materials without inclusions) using a rotational rheometer.

2.3 Machine Learning Constitutive Models

There have been methods using machine learning to learn the constitutive models for elasticity and plasticity, e.g., the work of Vlassis and Sun [2021], As'ad et al. [2022], Koeppe et al. [2022], and Li et al. [2022]. We note that the input and goal in these works are in general different from ours. They learn the constitutive relation from strain-stress data or simulated data, in order to obtain a macroscopic model from data in microscopic scales, or to accelerate the simulations. In contrast, ours takes a few real footage as input and returns the material parameters in order to reduce the manual workload needed for parameter tweaking. In addition, there are methods learning constitutive models using observations [Huang et al. 2020; Ma et al. 2023; Wang et al. 2020]. Compared to them, our method handles *rate-dependent* (non-Newtonian) rheology.

3 PROBLEM SETTING

3.1 Estimation as Optimization

Suppose that we have a material with a set of ground truth (Herschel–Bulkley) parameters $\mathbf{M}^\star = (\eta^\star, n^\star, \sigma_{\mathrm{Y}}{}^\star)^\top$ *unknown* to the user, and that we *sequentially* perform a set of *physical experiments* with *known* setups[4] $\mathbb{S} := \{\mathbf{S}_j\}$, $1 \le j \le N$. For each setup, we take a video $\mathcal{V}^\star(\mathbf{M}^\star; \mathbf{S}_j)$ to record the flowing behavior of the material. Now, if we have a guess $\mathbf{M}$ for the material parameters, we can run a *simulation* with the same setup $\mathbf{S}_j$ to obtain the resulting video $\mathcal{V}(\mathbf{M}; \mathbf{S}_j)$, and measure the difference $\delta(\mathcal{V}(\mathbf{M}; \mathbf{S}_j), \mathcal{V}^\star(\mathbf{M}^\star; \mathbf{S}_j))$ between the videos, using some error metric $\delta(\cdot,\cdot)$ described soon. The idea is then to figure out the appropriate parameter set $\hat{\mathbf{M}}$ that minimizes the loss $\mathcal{L}(\mathbf{M}, \mathbf{M}^\star; \mathbb{S})$:

$$\hat{\mathbf{M}} = \operatorname*{argmin}_{\mathbf{M}} \mathcal{L}(\mathbf{M}, \mathbf{M}^\star; \mathbb{S}) = \operatorname*{argmin}_{\mathbf{M}} \frac{1}{N} \sum_{j=1}^{N} \mathcal{L}(\mathbf{M}, \mathbf{M}^\star; \mathbf{S}_j)$$
$$= \operatorname*{argmin}_{\mathbf{M}} \frac{1}{N} \sum_{j=1}^{N} \delta(\mathcal{V}(\mathbf{M}; \mathbf{S}_j), \mathcal{V}^\star(\mathbf{M}^\star; \mathbf{S}_j)). \quad (2)$$

Following Takahashi et al. [2019], we define difference $\delta(\cdot,\cdot)$ between the videos $\mathcal{V}(\mathbf{M}; \mathbf{S})$ and $\mathcal{V}^\star(\mathbf{M}^\star; \mathbf{S})$ to be the averaged difference between their *silhouettes*. Let $\{\mathcal{I}_f(\mathbf{M}; \mathbf{S})\}$ and $\{\mathcal{I}_f{}^\star(\mathbf{M}^\star; \mathbf{S})\}$ be the image sequences constituting the videos $\mathcal{V}(\mathbf{M}; \mathbf{S})$ and $\mathcal{V}^\star(\mathbf{M}^\star; \mathbf{S})$, respectively. Given an image $\mathcal{I}_f$ or $\mathcal{I}_f{}^\star$ from the video as the input, a silhouette extraction filter $s(\cdot)$ removes the background, extracts the interior region, and outputs a binary image, with 0 encoding the interior and 1 the exterior. The difference $\delta(\cdot,\cdot)$ is then computed as

$$\delta(\mathcal{V}(\mathbf{M}; \mathbf{S}), \mathcal{V}^\star(\mathbf{M}^\star; \mathbf{S})) = \frac{1}{N_{\mathrm{F}} N_{\mathrm{P}}} \sum_{f=1}^{N_{\mathrm{F}}} \left\| s\left(\mathcal{I}_f(\mathbf{M}; \mathbf{S})\right) - s\left(\mathcal{I}_f{}^\star(\mathbf{M}^\star; \mathbf{S})\right) \right\|^2, \quad (3)$$

where N_{P} and N_{F} are, respectively, the number of pixels of a single image and the number of frames, and the squared norm $\|\cdot\|^2$ is the sum of the squared pixel differences. To minimize the loss (2), we use CMA-ES [Hansen and Kern 2004] as in the work of Takahashi et al. [2019], to be less sensitive to noises[5], such as errors in setting up the experiment setups and those in the silhouette extraction filter $s(\cdot)$. We leave the incorporation of a differentiable approach, such as the work of Murthy et al. [2021], as future work.

3.2 Incorporating Herschel–Bulkley Materials

During our preliminary study, we identified two tasks for estimating the material parameters for the Herschel–Bulkley model. First, we realized that there is a mismatch between the previously used Herschel–Bulkley model [Yue et al. 2015] and the situation encountered in a rotational rheometer. We propose a modification for a better match in Section 4. Second, we found that using only a single setup would occasionally fail to obtain a reasonable estimation, as evidenced by our experiments (Section 7.2). We found that this 'indeterminacy' is due to the existence of a *similarity relation* in the loss landscapes (Section 5). Building on these insights we develop our method (Algorithm 1) for the estimation by selecting additional setups (detailed in Section 6).

[4]The previous method by Takahashi et al. [2019] is equivalent to the case of $N = 1$.
[5]Note that in real world experiments, it is not realistic trying to remove all sources of errors; rather, we would like to be *tolerant* to errors.

We limit the search scope of the parameters to the material space $\mathfrak{M}$, such that it covers diverse materials while we can observe flows of those materials using our experiment setups. The material space is linearly scaled to the unit cube $[0, 1]^3$, which we call the *normalized material space*, for the computation in CMA-ES as well as setup selection.

Algorithm 1 `ViRheometry`

Input: Specimen $\mathcal{S}$, number of setups N
Output: The estimated material parameters $\hat{\mathbf{M}}$
1: $\mathbf{S}_1 \leftarrow (\mathtt{Rand}(20\,\mathrm{mm} \le w \le 70\,\mathrm{mm}), \mathtt{Rand}(20\,\mathrm{mm} \le h \le 70\,\mathrm{mm}))$
2: $\mathcal{V}_1 \leftarrow \mathtt{Experiment}(\mathcal{S}, \mathbf{S}_1)$
3: $\check{\mathbf{M}}_1 \leftarrow \mathtt{CMA\text{-}ES}(\mathcal{V}_1; \mathrm{Initial} = \mathbf{M}_{\mathrm{Init}}; \Sigma = 1.0)$
4: **for** $k = 2$ to N **do**
5: $\quad \mathbf{S}_k \leftarrow \mathtt{SetupSelection}(\check{\mathbf{M}}_{k-1}, \{\mathbf{S}_1, \ldots, \mathbf{S}_{k-1}\})$
6: $\quad \mathcal{V}_k \leftarrow \mathtt{Experiment}(\mathcal{S}, \mathbf{S}_k)$
7: $\quad \check{\mathbf{M}}_k \leftarrow \mathtt{CMA\text{-}ES}(\mathcal{V}_1, \ldots, \mathcal{V}_k; \mathrm{Initial} = \check{\mathbf{M}}_{k-1}; \Sigma = (2/3)^{k-1})$
8: **end for**
9: **return** $\hat{\mathbf{M}} \leftarrow \check{\mathbf{M}}_N$

3.3 Experiment Setups – Dam-Break

For the class of experiment setups, we aim for the one that is easy to configure and has enough degrees of freedom to cover kinematically different cases. Popular benchmark setups for fluids in the literature include 1) dropping or injecting the material through a nozzle toward the floor [Nagasawa et al. 2019; Takahashi and Lin 2019], 2) pouring the material down an inclined channel [Pellegrino and Schippa 2018; Sáo et al. 2021], and 3) dam-break (or column collapse) (such as the Bostwick consistometer). In all of these three examples, the kinematical variation is realized by the variations in a) the ratio between the inertia and the gravity force and b) the volume ratio between *plug flow* (zero velocity gradient) and non-uniform (non-zero velocity gradient) regions. We choose dam-break because of its simplicity and ability to provide enough variation; we do not have to worry about clogging at a nozzle or carefully configuring the slope angle.

In our version of a dam-break, we initially pour the material into a cuboid region enclosed by a horizontal floor and four vertical walls (Figure 1). After initialization, one side of the vertical wall is released to allow the material to flow out of the enclosed region[6]. The depth (distance between side walls) of the cuboid is much less informative in our dam-break setting, which we fix to a constant value (4.0 cm) throughout, and we define the set of setup parameters $\mathbf{S}$ to be the pair of the width w and height h of the initial cuboid geometry: $\mathbf{S} = (w, h)$ (as in Figure 8 (a)). For the specimens we used, we can assume non-slip boundary conditions.

For the candidates of the setups, we limit $20\,\mathrm{mm} \le w, h \le 70\,\mathrm{mm}$; we avoid too small setups to mitigate the effect of surface tension, boundary conditions and uneven free surfaces, while avoiding too big setups to save the amount of materials. Further, we limit the resolution for searching for the width w and height h to 1 mm, as

[6]After flowing out, the fluids can flow toward the sides, as opposed to regular dam-break settings where the side walls extend out. This is for reducing possible boundary effects due to the side walls.

finely tuning them is not realistic. This defines a discrete set of experiment setups $\mathbb{S}_{\text{exp}}$.

4 SIMULATING HERSCHEL–BULKLEY MATERIALS

We use an elasto-viscoplastic Herschel–Bulkley model as in the work of Yue et al. [2015] and Nagasawa et al. [2019]. As we try to estimate the three parameters η, n, and σ_{Y} for the flowing part only, we clarify the effect of elasticity and the conditions in which our approach works. In addition, we modify the model by Yue et al. [2015] for compatibility with the simple shear flow encountered in a rotational rheometer. Although the modifications in hindsight were only in coefficients in (14) and (15), they were important for matching up the results (Figure 4). To ease the discussion, we start from reviewing a 1D version corresponding to the *shear part* of a 3D model and move on to the 3D simple shear model. We then discuss the general 3D case and verify that the general case preserves the properties we see in the 1D model and the simple shear flow.

4.1 1D Elasto-viscoplastic Herschel–Bulkley Model

In 1D, we decompose the total *strain* ε into the elastic ε_{e} and plastic ε_{p} parts *additively*: $\varepsilon = \varepsilon_{\mathrm{e}} + \varepsilon_{\mathrm{p}}$. For the elastic part[7], we relate the strain ε_{e} with the stress σ_{s} using an elastic modulus μ:

$$\sigma_{\mathrm{s}} = \mu \varepsilon_{\mathrm{e}}. \tag{4}$$

When the stress from the elastic part exceeds the *yield stress* σ_{Y}, the excess deformation results in a permanent plastic flow, and excess stress σ_{ex} arises due to the viscosity applied to the plastic rate of strain $\dot{\varepsilon}_{\mathrm{p}}$. In the Herschel–Bulkley model, σ_{ex} is given by a power law:

$$\sigma_{\mathrm{ex}} = \sigma_{\mathrm{s}} - \sigma_{\mathrm{Y}} = \eta \dot{\varepsilon}_{\mathrm{p}}^{n}. \tag{5}$$

Subject to a prescribed constant rate $\dot{\varepsilon}$ of total strain (i.e., pulling the material at a constant speed), we must have

$$\dot{\varepsilon}_{\mathrm{p}} = \dot{\varepsilon} - \dot{\varepsilon}_{\mathrm{e}}. \tag{6}$$

As the strain is increased and the stress is past the yield stress, the plastic rate of strain starts to show up and there will be a *transient regime* where both rates of elastic and plastic strains are non-zero. During this transition regime, the rate of elastic strain gradually decreases, reaching a terminal state $\dot{\varepsilon}_{\mathrm{e}} \to 0$, hence $\dot{\varepsilon}_{\mathrm{p}} \to \dot{\varepsilon}$. Therefore, as the terminal stress $\sigma_{\mathrm{s},\infty}$, we have

$$\sigma_{\mathrm{s},\infty} = \sigma_{\mathrm{Y}} + \eta \dot{\varepsilon}^{n}. \tag{7}$$

As the ratio between a stress (σ_{ex}) and an elastic modulus (μ) is a strain, dividing it by the strain rate ($\dot{\varepsilon}$) suggests a *transition time* (for the prescribed strain rate $\dot{\varepsilon}$ to push the stress from σ_{Y} to $\sigma_{\mathrm{s},\infty}$):

$$t_{\infty} = \frac{\sigma_{\mathrm{ex}}}{\mu \dot{\varepsilon}} = \frac{\eta}{\mu \dot{\varepsilon}^{1-n}}. \tag{8}$$

From numerical analysis (shown in Figure 2) using (4), (5), and (6), we see that we indeed obtain the terminal stress and that t_{∞} seems to serve as a rough estimate of the time for the transition. It is important to understand that as μ becomes larger, the transition time t_{∞} reduces and the elastic strain approaches 0 (as σ_{Y} is fixed). At the limit, the above elasto-viscoplastic Herschel–Bulkley (*solid*) model becomes a Herschel–Bulkley *fluid*. In our simulation, we set $\mu = 10^3$ Pa so that the transition time is negligible (for the mean strain rate in the flow) compared to the 1/3 seconds for video recording, and at the same time the simulation does not require too small time steps for explicit integration. This would still include many fluid-like materials (as 10^3 Pa is usually considered to be on the 'softer' side) but exclude fluffy ones like shaving foam.

[7]We are re-using the symbols σ_{s} (shear stress) and μ (shear modulus) because this 1D model corresponds to the shear part of the 3D case.

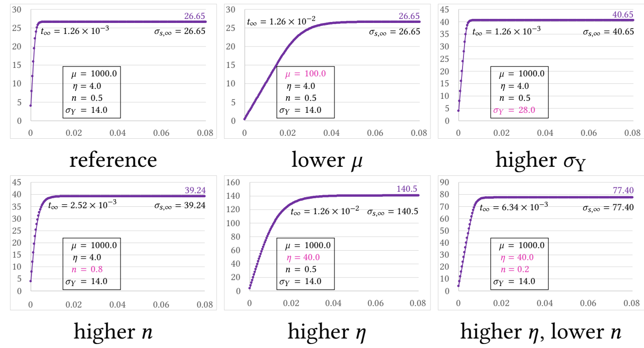

Fig. 2. **The evolution of stress (vertical) with respect to time (horizontal) for 1D flow rule.** We compare the transition time t_{∞} and terminal stress $\sigma_{\mathrm{s},\infty}$ predicted using (8) and (7) from the parameters shown in each plot, with the transient regime seen in the plot and the actual terminal stress shown in purple. $\dot{\varepsilon}$ is fixed to 10.0, a value within the range of shear rates encountered during the measurement using a rotational rheometer. From the parameter set shown in the top left plot, we are changing the parameter(s) in pink in the other plots.

4.2 3D Elasto-viscoplastic Model

To account for finite deformation in 3D, we incorporate multiplicative decomposition instead of the additive decomposition, which is an infinitesimal approximation of the multiplicative one[8]. The deformation from the reference configuration $\boldsymbol{X}$ to the current configuration $\boldsymbol{x}$ is described by the placement map $\phi : \boldsymbol{X} \mapsto \boldsymbol{x}$, which induces the so called deformation gradient $\mathbf{F} = \frac{\partial \phi(\boldsymbol{X})}{\partial \boldsymbol{X}}$ essentially describing the local coordinate transformation. With the multiplicative decomposition, $\mathbf{F}$ is decomposed to its elastic part $\mathbf{F}_{\mathrm{e}}$ and plastic part $\mathbf{F}_{\mathrm{p}}$: $\mathbf{F} = \mathbf{F}_{\mathrm{e}}\mathbf{F}_{\mathrm{p}}$. While $\mathbf{F}_{\mathrm{e}}$ encodes all the information of elastic deformation, computationally we should instead use a descriptor of deformation that provides *objectivity* or frame-indifference [Simo and Hughes 1998]; the reproduced physical behavior should not be affected by the coordinates we introduce. To handle rate-dependent plasticity, we need objectivity for not only strain but also strain rate. The (elastic part of the) left Cauchy–Green tensor $\mathbf{b}_{\mathrm{e}} = \mathbf{F}_{\mathrm{e}}\mathbf{F}_{\mathrm{e}}^{\top}$ and its Lie derivative $\mathcal{L}_{\boldsymbol{v}}\mathbf{b}_{\mathrm{e}}$ with respect to the velocity field $\boldsymbol{v}$ serve as such objective variables [Simo and Hughes 1998]. $\mathbf{b}_{\mathrm{e}}$ and $\mathcal{L}_{\boldsymbol{v}}\mathbf{b}_{\mathrm{e}}$ are related via

$$\dot{\mathbf{b}}_{\mathrm{e}} = \mathbf{L}\mathbf{b}_{\mathrm{e}} + \mathbf{b}_{\mathrm{e}}\mathbf{L}^{\top} + \mathcal{L}_{\boldsymbol{v}}\mathbf{b}_{\mathrm{e}}, \tag{9}$$

where $\mathbf{L}$ is the velocity gradient. Intuitively, (9) states that the update of $\mathbf{b}_{\mathrm{e}}$ involves an elastic part $\mathbf{L}\mathbf{b}_{\mathrm{e}} + \mathbf{b}_{\mathrm{e}}\mathbf{L}^{\top}$ due to the change in the

[8]When the elastic and plastic deformations are small, writing $\mathbf{F}_{\mathrm{e}} = (\mathbf{I} + \Delta\mathbf{F}_{\mathrm{e}})$ and $\mathbf{F}_{\mathrm{p}} = (\mathbf{I} + \Delta\mathbf{F}_{\mathrm{p}})$ yields $\mathbf{F}_{\mathrm{e}}\mathbf{F}_{\mathrm{p}} = \mathbf{I} + \Delta\mathbf{F}_{\mathrm{e}} + \Delta\mathbf{F}_{\mathrm{p}} + \Delta\mathbf{F}_{\mathrm{e}}\Delta\mathbf{F}_{\mathrm{p}} \approx \mathbf{I} + \Delta\mathbf{F}_{\mathrm{e}} + \Delta\mathbf{F}_{\mathrm{p}}$, where $\Delta\mathbf{F}_{\mathrm{e}}$ and $\Delta\mathbf{F}_{\mathrm{p}}$ correspond to ε_{e} and ε_{p}, respectively.

deformation enforced by the surrounding velocity field, as well as a plastic part $\mathcal{L}_{\boldsymbol{v}}\mathbf{b}_{\mathrm{e}}$ atop the elastic change.

Under finite deformation, the *linear* elasticity in the above 1D example is extended to a nonlinear *hyperelastic* model through a stored (or strain) energy density $\psi(\mathbf{b}_{\mathrm{e}})$, which relates the strain $\mathbf{b}_{\mathrm{e}}$ and stress $\boldsymbol{\sigma}$ via (10). The yield condition separating the elastic and plastic regimes is specified via a yield function $\Phi(\boldsymbol{\sigma};\sigma_{\mathrm{Y}})$ with $\Phi(\boldsymbol{\sigma};\sigma_{\mathrm{Y}}) \leq 0$ indicating the elastic regime. $\psi(\mathbf{b}_{\mathrm{e}})$, $\Phi(\boldsymbol{\sigma};\sigma_{\mathrm{Y}})$, together with a plastic flow model (called *flow rule*) for $\mathcal{L}_{\boldsymbol{v}}\mathbf{b}_{\mathrm{e}}$ characterize our 3D elasto-viscoplastic model.

From an argument regarding energy dissipation [Simo and Miehe 1992] (summarized in Appendix A for completeness), we have the elastic constitutive relation[9]

$$\boldsymbol{\sigma} = \frac{2}{J}\frac{\partial \psi}{\partial \mathbf{b}_{\mathrm{e}}}\mathbf{b}_{\mathrm{e}}, \tag{10}$$

where $J = \det[\mathbf{F}_{\mathrm{e}}]$, as well as the flow rule

$$-\frac{1}{2}(\mathcal{L}_{\boldsymbol{v}}\mathbf{b}_{\mathrm{e}}){\mathbf{b}_{\mathrm{e}}}^{-1} = \lambda\frac{\partial \Phi}{\partial \boldsymbol{\sigma}}, \tag{11}$$

where λ is the flow rate (In §4.3, we will replace λ with $\dot{\gamma}_{\mathrm{HB}}$ in (17), and in §4.4, we see the validity of this replacement[10]).

For the stored energy density $\psi(\mathbf{b}_{\mathrm{e}})$, we use the following version as in the work of Simo and Hughes [1998] and Yue et al. [2015]:

$$\psi(\mathbf{b}_{\mathrm{e}}) = \frac{1}{2}\kappa\left(\frac{1}{2}(J^2-1) - \log J\right) + \frac{1}{2}\mu(\mathrm{tr}[\bar{\mathbf{b}}_{\mathrm{e}}] - d), \tag{12}$$

where κ and μ are the bulk and shear moduli, respectively, d is the dimensionality, and $\bar{\mathbf{b}}_{\mathrm{e}} = J^{-2/d}\mathbf{b}_{\mathrm{e}}$ is the volume-factored version of $\mathbf{b}_{\mathrm{e}}$. We set κ to be sufficiently large[11] ($\kappa = 10^4$ Pa) so that $J \approx 1$. The shear stress $\boldsymbol{\sigma}_{\mathrm{s}}$ is given by

$$\boldsymbol{\sigma}_{\mathrm{s}} = \mathrm{dev}[\boldsymbol{\sigma}] = \frac{\mu}{J}\,\mathrm{dev}[\bar{\mathbf{b}}_{\mathrm{e}}], \tag{13}$$

where $\mathrm{dev}[\mathbf{x}] := \mathbf{x} - \frac{1}{d}\,\mathrm{tr}[\mathbf{x}]\mathbf{I}$ is the deviatoric operator. We have $\mathrm{tr}[\mathrm{dev}[\mathbf{x}]] = 0$, $\mathrm{dev}[\mathbf{I}] = \mathbf{O}$, and $\mathrm{dev}[\mathrm{dev}[\mathbf{x}]] = \mathrm{dev}[\mathbf{x}]$, where $\mathbf{I}$ and $\mathbf{O}$ are the identity and zero tensors, respectively.

In Figure 3, we see that increasing the elastic moduli only slightly alters the simulated shapes compared to our choice of the elastic moduli ($\kappa = 10^4$ Pa, $\mu = 10^3$ Pa). Note that we claim the validity of this choice only for our purpose, not for other types of flows (and materials) in general.

4.3 Matching Yield Function and Flow Rule

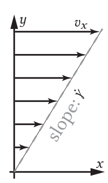

We determine the yield function $\Phi(\boldsymbol{\sigma};\sigma_{\mathrm{Y}})$ and λ in (11) to match the *simple shear* flow applied to the specimen in a rotational rheometer. Consider a simple shear along the x axis with the *constant* velocity gradient $\dot{\gamma}$ occurring in the y axis (as in the inset)[12]. Let the components of the velocity be $\boldsymbol{v} = (v_x, v_y)^{\top}$ in 2D and $\boldsymbol{v} = (v_x, v_y, v_z)$ in 3D. The above simple shear states that $v_y = 0$, $v_z = 0$, and $\frac{\partial v_\cdot}{\partial \cdot} = 0$ except that $\frac{\partial v_x}{\partial y} = \dot{\gamma} \geq 0$. Let $\mathbf{L}_{\mathrm{I}} = \begin{pmatrix} 0 & 1 & 0 \\ 0 & 0 & 0 \\ 0 & 0 & 0 \end{pmatrix}$ (or $\mathbf{L}_{\mathrm{I}} = \begin{pmatrix} 0 & 1 \\ 0 & 0 \end{pmatrix}$ in 2D) be the 'unit' velocity gradient. Then, the velocity gradient $\mathbf{L}$ in a simple shear is $\mathbf{L} = \dot{\gamma}\mathbf{L}_{\mathrm{I}}$. Likewise, defining $\mathbf{D}_{\mathrm{I}} := \mathbf{L}_{\mathrm{I}} + \mathbf{L}_{\mathrm{I}}^{\top}$, the induced shear stress $\boldsymbol{\sigma}_{\mathrm{s}}$ can be written using a scalar shear stress σ_{s} as $\boldsymbol{\sigma}_{\mathrm{s}} = \sigma_{\mathrm{s}}\mathbf{D}_{\mathrm{I}}$.

The flow curve measured by a rotational rheometer states the scalar relation between $\dot{\gamma}$ and σ_{s}. For later ease of notation, we define a shear rate tensor $\mathbf{D} = 2\mathbf{d} = \mathbf{L} + \mathbf{L}^{\top}$ ($\mathbf{d}$ is used in Appendix A). Then, we have the following conversions (extracting the off diagonal terms) from the tensors of shear rate and shear stress to their scalar counterpart:

$$\dot{\gamma} = \sqrt{\frac{\mathbf{D}:\mathbf{D}}{2}} = \frac{1}{\sqrt{2}}\|\mathbf{D}\|_{\mathrm{F}}, \quad \sigma_{\mathrm{s}} = \sqrt{\frac{\boldsymbol{\sigma}_{\mathrm{s}}:\boldsymbol{\sigma}_{\mathrm{s}}}{2}} = \frac{1}{\sqrt{2}}\|\boldsymbol{\sigma}_{\mathrm{s}}\|_{\mathrm{F}}, \tag{14}$$

where $\|\cdot\|_{\mathrm{F}}$ is the Frobenius norm. The factor $\frac{1}{\sqrt{2}}$ appears to cancel the Frobenius norm of $\mathbf{D}_{\mathrm{I}}$, which was missing in the work of Yue et al. [2015].

As for the yield condition, the scalar stress σ_{s} is directly compared with the yield stress σ_{Y}. Since $\boldsymbol{\sigma}_{\mathrm{s}} = \mathrm{dev}[\boldsymbol{\sigma}]$, we have the following (von-Mises type) yield function (same for both 2D and 3D):

$$\boxed{\Phi(\boldsymbol{\sigma};\sigma_{\mathrm{Y}}) = \frac{1}{\sqrt{2}}\|\,\mathrm{dev}[\boldsymbol{\sigma}]\|_{\mathrm{F}} - \sigma_{\mathrm{Y}}.} \tag{15}$$

Unlike the work of Yue et al. [2015], we do not have the usual $\sqrt{3}$ factor; the standard von-Mises is defined for pure shear (rather than simple shear) and tensile stress. The flow direction is then computed as

$$\frac{\partial \Phi}{\partial \boldsymbol{\sigma}} = \frac{1}{\sqrt{2}}\frac{\mathrm{dev}[\boldsymbol{\sigma}]}{\|\,\mathrm{dev}[\boldsymbol{\sigma}]\|_{\mathrm{F}}}, \tag{16}$$

which in the simple shear is just $\mathbf{D}_{\mathrm{I}}$.

To derive the flow rule, we set the flow rate $\dot{\gamma}_{\mathrm{HB}}$ to update the elastic strain (measure) $\mathbf{b}_{\mathrm{e}}$ according to the Herschel–Bulkley model (1):

$$\dot{\gamma}_{\mathrm{HB}} = \left(\frac{\max(0, \sigma_{\mathrm{s}} - \sigma_{\mathrm{Y}})}{\eta}\right)^{1/n}. \tag{17}$$

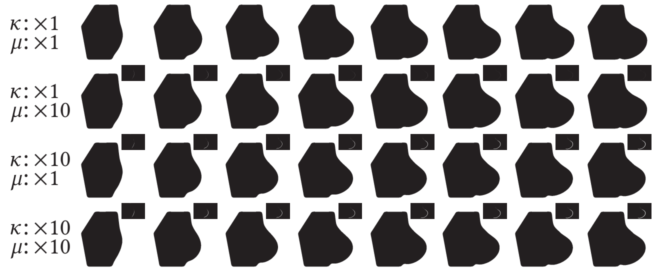

Fig. 3. **Comparison of different elastic moduli (κ, μ) settings.** The insets show the image differences with the corresponding image of the case κ : ×1 and μ : ×1.

[9] The relation (10) is equivalent to the usual relation $\boldsymbol{\sigma} = \frac{1}{J}\frac{\partial \psi}{\partial \mathbf{F}_{\mathrm{e}}}{\mathbf{F}_{\mathrm{e}}}^{\top}$.

[10] The argument regarding energy dissipation only asserts that the flow direction (left side of (11)) is parallel to $\frac{\partial \Phi}{\partial \boldsymbol{\sigma}}$, so we need to verify that replacing λ with $\dot{\gamma}_{\mathrm{HB}}$ gives the right flow rate.

[11] Like the choice for μ, this is just enough for negligible volume change in terms of the visual, while allowing for not too small time steps for explicit integration.

[12] Ideally, a rotational rheometer applies a flow with constant velocity gradient to the specimen. By choosing the coordinates appropriately, we can consider a simple shear in the xy space.

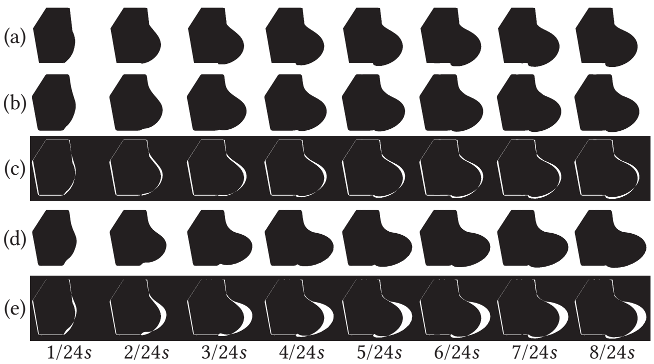

Fig. 4. **Comparison between flow rules.** (a): Binary image of the captured footage for the moisturizing milk example shown in Section 7.2, (b): simulated with our flow rule, (c): difference between (a) and (b), (d): simulated with the model by Yue et al. [2015], (e): difference between (a) and (d). For the simulations (b) and (d), we used the material parameters measured by a rotational rheometer. While ours (b) shows nice agreement with the captured footage, (d) flows notably faster than it should.

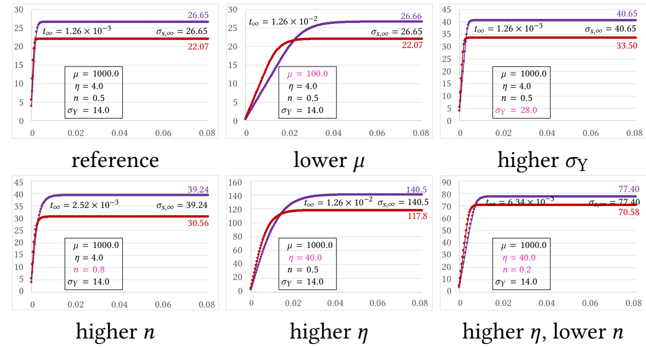

Fig. 5. **The evolution of stress (vertical) with respect to time (horizontal) for 3D simple shear.** We compare our modified flow rule (purple line) with that of Yue et al. [2015] (red line). Our rule provides the right terminal stress $\sigma_{s,\infty}$, whereas that of Yue et al. [2015] results in a lower terminal stress. $\dot{\gamma}$ is fixed to 10.0 as in Figure 2. From the parameter set shown in the top left plot, we are changing the parameter(s) in pink in the other plots.

Like the distinction between $\dot{\varepsilon}$ and $\dot{\varepsilon}_p$ made in the 1D case, we need to distinguish the shear rate $\dot{\gamma}$ (due to the velocity gradient) and the flow rate $\dot{\gamma}_{HB}$ (due to the plastic flow) when there is elasticity. Putting everything (11), (16), and (17) together (replacing λ with $\dot{\gamma}_{HB}$), we have the following flow rule:

$$\boxed{\mathcal{L}_{\boldsymbol{v}}\mathbf{b}_e = -\dot{\gamma}_{HB}\left(\sqrt{2}\frac{\mathrm{dev}[\boldsymbol{\sigma}]}{\|\mathrm{dev}[\boldsymbol{\sigma}]\|_F}\right)\mathbf{b}_e.} \tag{18}$$

4.4 Properties of the Flow Rule

We see two properties of the flow rule. First, as the terminal state (when $\dot{\mathbf{b}}_e = \mathbf{O}$) for a simple shear, we have $\dot{\gamma}_{HB} = \dot{\gamma}$ like the 1D case. This is because for μ sufficiently large, $\mathbf{b}_e$ is close to identity so $(\mathcal{L}_{\boldsymbol{v}}\mathbf{b}_e)\mathbf{b}_e^{-1} \approx -(\mathbf{L}+\mathbf{L}^\top) = -\mathbf{D} = -\dot{\gamma}\mathbf{D}_I$, and that the flow direction (16) is $\mathbf{D}_I$ in the simple shear. Thus, λ in (11) was indeed the flow rate and the replacement was valid. We also see this fact from numerical experiment (using (9), (10), (15), (18), and $\mathbf{L} = \dot{\gamma}\mathbf{L}_I$ with $\dot{\gamma} = 10.0$) shown in Figure 5 (purple lines). Comparing the purple lines in Figures 2 and 5, the agreement with the 1D version shows that the 3D version is a nice extension of the 1D model. We also note that the constitutive model by Yue et al. [2015] results in a substantially lower terminal stress, giving faster flow than expected as in Figure 4. Ours provides better agreement with the captured footage. The agreement can also be seen from Figure 1, where the simulated results nicely reproduce the 'shoulder' seen in the captured footage for congee. Second, the flow rule (18) is volume preserving, because during the update (18) we have $\frac{d}{dt}\det[\mathbf{b}_e] = \frac{d\det[\mathbf{b}_e]}{d\mathbf{b}_e} : \mathcal{L}_{\boldsymbol{v}}\mathbf{b}_e = 0$ (hence $\dot{J} = 0$ also).

A discrete *return mapping* algorithm should ideally preserve the above two properties. We show in Appendix B that a slight modification to the version of Yue et al. [2015] suffices. The computation cost of the discrete return mapping using our modified version is almost identical to that using the version of Yue et al. [2015], as the modification is essentially in the coefficients.

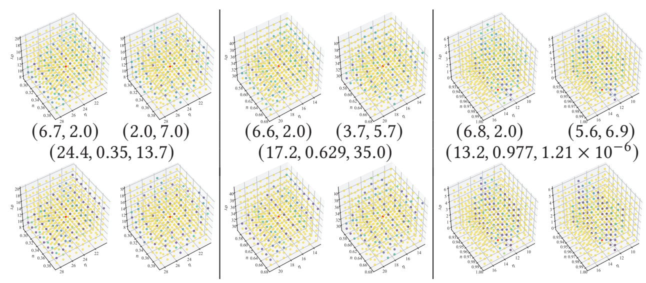

Fig. 6. **MPM 3D loss (top) and the matched plane Poiseuille loss (bottom)** for different material-setup pairs. Red dots indicate the ground truth material parameters (η, n, σ_Y) shown in the middle. Setups are shown in (width, height).

5 SIMILARITY STRUCTURE AND ANALYSIS

Toward the optimizations for the material parameters, we draw insights for the loss functions. We analyze the loss function for a single setup $\mathcal{L}(\mathbf{M}, \mathbf{M}^\star; \mathbf{S})$ in (2) and reveal its *similarity structure* (§5.1), the source of indeterminacy where low loss values are located. We show how this structure can be mathematically defined (via *Hessian* and *loss normal*, §5.2) and computed (§5.3). For efficiently estimating the loss normals, we establish a relation between our loss $\mathcal{L}(\mathbf{M}, \mathbf{M}^\star; \mathbf{S})$ and another loss function of an idealized steady flow, which admits an analytical form of its similarity structure (§5.4 and §5.5). This relation will be used to propose setups for experiments in §6.

5.1 Loss Landscapes

To see the structure of the loss landscapes, we sampled in total 200 landscapes $\mathfrak{L}$, by first using Poisson disk sampling to draw 20 materials from the material space $\mathfrak{M}$, and then randomly sampling 10 setups from the setup space $\mathbb{S}_{\mathrm{exp}}$ for each of the material. For each of the material-setup pairs, we performed MPM 3D simulations

Fig. 7. **Loss landscapes and silhouette images for different views** (top and bottom). Note the silhouette images can be quite similar even if the material parameters are far apart.

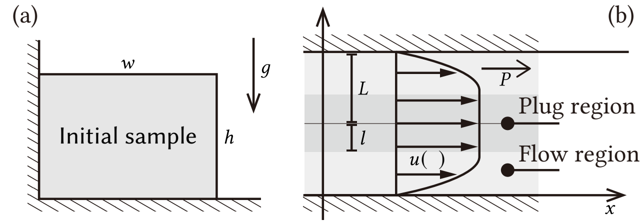

Fig. 8. (a) A dam-break setup. (b) A plane Poiseuille flow setup.

to compute loss values at 512 points regularly aligned (in the normalized material space) at the vicinity of the ground truth material parameters (Figure 6 Top; see our supplementary material A §6 for all the landscapes). The view used to compute the losses is shown in Figure 7 Top. From this *local* analysis, we see that for every material-setup pair, there is a thin, low loss region, which we call *similarity set*, indicating an indeterminacy of the material parameters within that region; different material parameters result in almost identical silhouettes (Figure 7, supplementary material A §7). In addition, there is a dependence of the orientation of that region on the setups (the magnitudes of the dependency relies on the materials). We see that changing the view as in Figure 7 (and supplementary material A §7) had little impact on the loss structure[13].

5.2 Hessian as a Similarity Measure

Mathematically, we define the similarity set $\mathbb{M}_{\mathbf{M}}(\mathrm{S})$ for a given setup S and the material parameters $\mathbf{M}$ as

$$\mathbb{M}_{\mathbf{M}}(\mathrm{S}) := \{\tilde{\mathbf{M}} \mid \mathcal{L}(\tilde{\mathbf{M}}, \mathbf{M}; \mathrm{S}) \le \mathcal{T}\}, \tag{19}$$

where $\mathcal{T}$ is a threshold for the (small) loss value. As we will see, the Hessian of the loss characterizes this similarity set. Let $\tilde{\mathbf{M}} = \mathbf{M} + \Delta\mathbf{M}$, where $\Delta\mathbf{M}$ is a small variation in the material space, and $\mathcal{L}_{\mathbf{M};\mathrm{S}}(\tilde{\mathbf{M}}) := \mathcal{L}(\tilde{\mathbf{M}}, \mathbf{M}; \mathrm{S})$. We obtain the Taylor expansion of the loss as

$$\mathcal{L}_{\mathbf{M};\mathrm{S}}(\tilde{\mathbf{M}}) = \mathcal{L}_{\mathbf{M};\mathrm{S}}(\mathbf{M}) + G_{\mathbf{M};\mathrm{S}}\Delta\mathbf{M} + \Delta\mathbf{M}^\top \mathbf{H}_{\mathbf{M};\mathrm{S}}\Delta\mathbf{M} + O(|\Delta\mathbf{M}|^3), \tag{20}$$

where $G_{\mathbf{M};\mathrm{S}} := \left.\frac{\partial \mathcal{L}_{\mathbf{M};\mathrm{S}}}{\partial \tilde{\mathbf{M}}}\right|_{\tilde{\mathbf{M}}=\mathbf{M}}$ and $\mathbf{H}_{\mathbf{M};\mathrm{S}} := \left.\frac{\partial^2 \mathcal{L}_{\mathbf{M};\mathrm{S}}}{\partial \tilde{\mathbf{M}}^\top \partial \tilde{\mathbf{M}}}\right|_{\tilde{\mathbf{M}}=\mathbf{M}}$ for the gradient and Hessian of the loss, respectively. Because the loss is zero and minimum at $\tilde{\mathbf{M}} = \mathbf{M}$, we have $\mathcal{L}_{\mathbf{M};\mathrm{S}}(\mathbf{M}) = 0$ and $G_{\mathbf{M};\mathrm{S}} = \mathbf{0}^\top$. Hence, the loss is locally characterized by the Hessian $\mathbf{H}_{\mathbf{M};\mathrm{S}}$:

$$\mathcal{L}(\tilde{\mathbf{M}}, \mathbf{M}; \mathrm{S}) \le \mathcal{T} \Leftrightarrow \Delta\mathbf{M}^\top \mathbf{H}_{\mathbf{M};\mathrm{S}}\Delta\mathbf{M} \le \mathcal{T} + O(|\Delta\mathbf{M}|^3). \tag{21}$$

Let $\mathbf{H}_{\mathbf{M};\mathrm{S}} = \mathbf{Q}^\top_{\mathbf{M};\mathrm{S}}\mathbf{\Lambda}_{\mathbf{M};\mathrm{S}}\mathbf{Q}_{\mathbf{M};\mathrm{S}}$ be the eigendecomposition of the Hessian, where $\mathbf{Q}_{\mathbf{M};\mathrm{S}}$ consists of eigenvectors and $\mathbf{\Lambda}_{\mathbf{M};\mathrm{S}} = \mathrm{diag}(\lambda_1, \lambda_2, \lambda_3)$ consists of eigenvalues λ_1, λ_2, and λ_3. The similarity set then becomes

$$\mathbb{M}_{\mathbf{M}}(\mathrm{S}) \approx \{\tilde{\mathbf{M}} \mid (\mathbf{Q}_{\mathbf{M};\mathrm{S}}(\tilde{\mathbf{M}} - \mathbf{M}))^\top \mathbf{\Lambda}_{\mathbf{M};\mathrm{S}}(\mathbf{Q}_{\mathbf{M};\mathrm{S}}(\tilde{\mathbf{M}} - \mathbf{M})) \le \mathcal{T}\}, \tag{22}$$

which reveals its *ellipsoidal* structure, with its axes given by the eigenvectors, while the length l_i along the i-th eigenvector given by $l_i = \sqrt{\mathcal{T}|\lambda_i|^{-1}}$. The shortest axis (i.e., the direction the material parameters are most accurately determined, or, the *normal* direction of the similarity set) is characterized by the eigenvector $\boldsymbol{q}_{\max}$ corresponding to the *largest eigenvalue*. We call $\boldsymbol{q}_{\max}$ the *loss normal*.

5.3 Toward the Estimation of the Loss Normal

To estimate $\mathbf{H}_{\mathbf{M};\mathrm{S}}$, one possibility is to make all the processes (i.e., from simulation to surface extraction and rendering) encapsulated in the computation of the loss function differentiable, which should be a viable future work. Another possibility is to use finite differences, which is however costly[14]. In addition, we note that the loss normals estimated using finite differences usually seem to be accurate, but can be noisy (unreliable) for materials with extremely low yield stress (like honey). Instead, we analyzed the plane Poiseuille flow for Herschel–Bulkley fluids and found their Hessians $\mathbf{H}^{\mathrm{PP}}$ can be computed analytically. We establish a connection between the (unsteady) dam-break (DB) and (steady) plane Poiseuille (PP) flows, and show that we can learn a function Θ that maps the pair of the material parameter set $\mathbf{M}$ and the DB setup S to a PP setup S^{PP}: $\mathrm{S}^{\mathrm{PP}} = \Theta(\mathbf{M}, \mathrm{S})$, allowing for light weight and accurate estimation of the loss normal[15] $\boldsymbol{q}_{\max}$ through $\mathbf{H}^{\mathrm{PP}}$ (Algorithm 2).

Algorithm 2 `Loss_Normal_Estimation`

Input: A material estimate $\hat{\mathbf{M}}$ and a dam-break setup S
Output: The estimated loss normal $\boldsymbol{q}_{\max\hat{\mathbf{M}};\mathrm{S}}$

1: $\mathrm{S}^{\mathrm{PP}} \leftarrow \Theta(\hat{\mathbf{M}}, \mathrm{S})$
2: $\mathbf{H}^{\mathrm{PP}}_{\hat{\mathbf{M}};\mathrm{S}^{\mathrm{PP}}} \leftarrow$ `Compute_Hessian`$(\hat{\mathbf{M}}, \mathrm{S}^{\mathrm{PP}})$
3: $\boldsymbol{q}^{\mathrm{PP}}_{\max\hat{\mathbf{M}};\mathrm{S}^{\mathrm{PP}}} \leftarrow$ `Eigendecomposition`$(\mathbf{H}^{\mathrm{PP}}_{\hat{\mathbf{M}};\mathrm{S}^{\mathrm{PP}}})$
4: **return** $\boldsymbol{q}_{\max\hat{\mathbf{M}};\mathrm{S}} \leftarrow \boldsymbol{q}^{\mathrm{PP}}_{\max\hat{\mathbf{M}};\mathrm{S}^{\mathrm{PP}}}$

5.4 Herschel–Bulkley plane Poiseuille Flow and its Hessian

We consider a channel flow between two infinitely long non-slip plates placed in parallel separated by a distance of $2L$. Assuming the flow extends in parallel in the depth dimension, it suffices to consider a 2D slice. By applying a constant *pressure gradient* P along the direction parallel to the plates (as in Figure 8 (b)) and with

[13]We believe that a good view is a one, like ours, that reflects the spread after flowing out and the change in the height and free surface (e.g., the shoulder in Figure 1).

[14]It is costly because more than tens of simulations are needed per a single estimation of a Hessian, and that we want to compare multiple Hessians to determine the next setup; it would result in hundreds of simulations per setup selection. Our approach in Section 6, in contrast, performs no simulation and can select a new setup within a second.

[15]We do not claim that $\mathbf{H}^{\mathrm{PP}}$ is an accurate approximation of $\mathbf{H}$, as their condition numbers do not match up well. Nonetheless, the loss normal seems useful for our purpose of ViRheometry.

no external force, a *steady* flow (2D plane Poiseuille flow) with a constant velocity profile irrespective of time is formed between the plates. This plane Poiseuille flow closely models the ideal flow occurring in a pipe rheometer. A setup of a plane Poiseuille flow can thus be represented by P and L as $\mathrm{S}^{\mathrm{PP}} := (P, L)$. In physics, the existence of analytical solutions for Bingham and Herschel–Bulkley fluids has been shown [Sankar and Lee 2016]. Our work builds on these insights.

We set the x- (resp. y-) axis parallel (resp. perpendicular) to the two infinite plates, and let the positions of the plates be $y = \pm L$, as in Figure 8 (b). As detailed in our supplementary material A §2, the flow solely occurs in the x direction, and the velocity $\boldsymbol{v}_{\mathbf{M};\mathrm{S}^{\mathrm{PP}}}$ can be written in the form $\boldsymbol{v}_{\mathbf{M};\mathrm{S}^{\mathrm{PP}}} = (v_{x,\mathbf{M};\mathrm{S}^{\mathrm{PP}}}(y), 0)$. In addition, there will be yield surfaces at $y = \pm l$ separating the flowing (non-zero velocity gradient) and plug (zero velocity gradient) regions, with l given by $l = \sigma_{\mathrm{Y}}/P$.

Writing the velocity profile $v_{x,\mathbf{M};\mathrm{S}^{\mathrm{PP}}}(y)$ as a product of two terms, one for the maximum velocity $v^{(\mathrm{Max})}_{x,\mathbf{M};\mathrm{S}^{\mathrm{PP}}}$ in the channel (occurring at the plug region) and the other for the velocity decay ratio $\zeta_{\mathbf{M};\mathrm{S}^{\mathrm{PP}}}(y)$ (between the velocity at y and the maximum velocity), we have

$$v_{x,\mathbf{M};\mathrm{S}^{\mathrm{PP}}}(y) = v^{(\mathrm{Max})}_{x,\mathbf{M};\mathrm{S}^{\mathrm{PP}}}\zeta_{\mathbf{M};\mathrm{S}^{\mathrm{PP}}}(y), \tag{23}$$

where the derivations (in our supplementary material A §3) show

$$v^{(\mathrm{Max})}_{x,\mathbf{M};\mathrm{S}^{\mathrm{PP}}} = \frac{n}{n+1}\left(\frac{P}{\eta}\right)^{1/n}(L-l)^{\frac{n+1}{n}}, \tag{24}$$

$$\zeta_{\mathbf{M};\mathrm{S}^{\mathrm{PP}}}(y) = 1 - \left(\frac{\max(0, |y| - l)}{L - l}\right)^{\frac{n+1}{n}}. \tag{25}$$

We define the loss for the plane Poiseuille flow $\mathcal{L}^{\mathrm{PP}}(\tilde{\mathbf{M}}, \mathbf{M}; \mathrm{S}^{\mathrm{PP}})$ for materials $\tilde{\mathbf{M}}$ and $\mathbf{M}$ as the squared error between their velocity profiles $v_{x,\tilde{\mathbf{M}};\mathrm{S}^{\mathrm{PP}}}(y)$ and $v_{x,\mathbf{M};\mathrm{S}^{\mathrm{PP}}}(y)$:

$$\mathcal{L}^{\mathrm{PP}}(\tilde{\mathbf{M}}, \mathbf{M}; \mathrm{S}^{\mathrm{PP}}) = \int_0^L \left(v_{x,\tilde{\mathbf{M}};\mathrm{S}^{\mathrm{PP}}}(y) - v_{x,\mathbf{M};\mathrm{S}^{\mathrm{PP}}}(y)\right)^2 dy, \tag{26}$$

where we are only integrating the error in the y direction for $0 \le y \le L$ because the velocity profiles are independent of the x position and are symmetric around $y = 0$.

We take a variational approach to compute the Hessian $\mathbf{H}^{\mathrm{PP}}_{\mathbf{M};\mathrm{S}^{\mathrm{PP}}}$ of the plane Poiseuille loss $\mathcal{L}^{\mathrm{PP}}(\tilde{\mathbf{M}}, \mathbf{M}, \mathrm{S}^{\mathrm{PP}})$. Let $\tilde{\mathbf{M}} = \mathbf{M} + \varepsilon\boldsymbol{\xi}$. Then, we expand $v_{x,\tilde{\mathbf{M}};\mathrm{S}^{\mathrm{PP}}}(y) = v_{x,\mathbf{M}+\varepsilon\boldsymbol{\xi};\mathrm{S}^{\mathrm{PP}}}(y)$ as

$$v_{x,\mathbf{M}+\varepsilon\boldsymbol{\xi};\mathrm{S}^{\mathrm{PP}}}(y) = v_{x,\mathbf{M};\mathrm{S}^{\mathrm{PP}}}(y) + \varepsilon\boldsymbol{G}_{\mathbf{M};\mathrm{S}^{\mathrm{PP}}}(y)\boldsymbol{\xi} + O(\varepsilon^2), \tag{27}$$

where $\boldsymbol{G}_{\mathbf{M};\mathrm{S}^{\mathrm{PP}}}(y) = \left.\frac{\partial v_{x,\tilde{\mathbf{M}};\mathrm{S}^{\mathrm{PP}}}(y)}{\partial \mathbf{M}}\right|_{\tilde{\mathbf{M}}=\mathbf{M}}$. Substituting into $\mathcal{L}^{\mathrm{PP}}$,

$$\mathcal{L}^{\mathrm{PP}}(\tilde{\mathbf{M}}, \mathbf{M}; \mathrm{S}^{\mathrm{PP}}) = \frac{1}{2}\varepsilon^2\boldsymbol{\xi}^\top\left[2\int_0^L \boldsymbol{G}_{\mathbf{M};\mathrm{S}^{\mathrm{PP}}}(y)^\top \boldsymbol{G}_{\mathbf{M};\mathrm{S}^{\mathrm{PP}}}(y)dy\right]\boldsymbol{\xi} + O(\varepsilon^3). \tag{28}$$

Differentiating with respect to ε and setting $\varepsilon = 0$ reveals $\mathbf{H}^{\mathrm{PP}}_{\mathbf{M};\mathrm{S}^{\mathrm{PP}}}$:

$$\boxed{\mathbf{H}^{\mathrm{PP}}_{\mathbf{M};\mathrm{S}^{\mathrm{PP}}} = 2\int_0^L \boldsymbol{G}_{\mathbf{M};\mathrm{S}^{\mathrm{PP}}}(y)^\top \boldsymbol{G}_{\mathbf{M};\mathrm{S}^{\mathrm{PP}}}(y)dy.} \tag{29}$$

Writing the components of $\mathbf{H}^{\mathrm{PP}}_{\mathbf{M};\mathrm{S}^{\mathrm{PP}}}$ as

$$\mathbf{H}^{\mathrm{PP}}_{\mathbf{M};\mathrm{S}^{\mathrm{PP}}} = L^3\tilde{\mathbf{H}}^{\mathrm{PP}}_{\mathbf{M};\mathrm{S}^{\mathrm{PP}}} = L^3\begin{pmatrix} \tilde{H}_{\eta\eta} & \tilde{H}_{\eta n} & \tilde{H}_{\eta\sigma_{\mathrm{Y}}} \\ \tilde{H}_{\eta n} & \tilde{H}_{nn} & \tilde{H}_{n\sigma_{\mathrm{Y}}} \\ \tilde{H}_{\eta\sigma_{\mathrm{Y}}} & \tilde{H}_{n\sigma_{\mathrm{Y}}} & \tilde{H}_{\sigma_{\mathrm{Y}}\sigma_{\mathrm{Y}}} \end{pmatrix}, \tag{30}$$

they can be computed analytically as

$$\tilde{H}_{\eta\eta} = 2\frac{\sigma_{\mathrm{Y}}}{PL}A_\eta^2 + 4\left(1 - \frac{\sigma_{\mathrm{Y}}}{PL}\right)A_\eta^2 C_1, \tag{31}$$

$$\tilde{H}_{\eta n} = 2\frac{\sigma_{\mathrm{Y}}}{PL}A_\eta A_n + 2\left(1 - \frac{\sigma_{\mathrm{Y}}}{PL}\right)\left(2A_\eta A_n C_1 - A_\eta B_n C_2\right), \tag{32}$$

$$\tilde{H}_{\eta\sigma_{\mathrm{Y}}} = 2\frac{\sigma_{\mathrm{Y}}}{PL}A_\eta A_{\sigma_{\mathrm{Y}}} + 2\left(1 - \frac{\sigma_{\mathrm{Y}}}{PL}\right)A_\eta A_{\sigma_{\mathrm{Y}}} C_3, \tag{33}$$

$$\tilde{H}_{nn} = 2\frac{\sigma_{\mathrm{Y}}}{PL}A_n^2 + 4\left(1 - \frac{\sigma_{\mathrm{Y}}}{PL}\right)\left(B_n^2 C_4 - A_n B_n C_2 + A_n^2 C_1\right), \tag{34}$$

$$\tilde{H}_{n\sigma_{\mathrm{Y}}} = 2\frac{\sigma_{\mathrm{Y}}}{PL}A_n A_{\sigma_{\mathrm{Y}}} + 2\left(1 - \frac{\sigma_{\mathrm{Y}}}{PL}\right)\left(A_n A_{\sigma_{\mathrm{Y}}} C_3 - B_n A_{\sigma_{\mathrm{Y}}} C_5\right), \tag{35}$$

$$\tilde{H}_{\sigma_{\mathrm{Y}}\sigma_{\mathrm{Y}}} = 2\frac{\sigma_{\mathrm{Y}}}{PL}A_{\sigma_{\mathrm{Y}}}^2 + 4\left(1 - \frac{\sigma_{\mathrm{Y}}}{PL}\right)A_{\sigma_{\mathrm{Y}}}^2 C_6, \tag{36}$$

where,

$$A_\eta = -\frac{1}{n+1}\frac{1}{PL}\left(\frac{PL - \sigma_{\mathrm{Y}}}{\eta}\right)^{\frac{n+1}{n}}, \quad A_{\sigma_{\mathrm{Y}}} = -\frac{1}{PL}\left(\frac{PL - \sigma_{\mathrm{Y}}}{\eta}\right)^{\frac{1}{n}}, \tag{37}$$

$$A_n = \frac{\eta}{PL}\left(\frac{PL - \sigma_{\mathrm{Y}}}{\eta}\right)^{\frac{n+1}{n}}\left(\frac{1}{(n+1)^2} - \frac{1}{n(n+1)}\left(\log\frac{PL - \sigma_{\mathrm{Y}}}{\eta}\right)\right), \tag{38}$$

$$B_n = \frac{1}{n(n+1)}\left(\frac{PL - \sigma_{\mathrm{Y}}}{\eta}\right)^{\frac{1}{n}}\left(1 - \frac{\sigma_{\mathrm{Y}}}{PL}\right), \tag{39}$$

and

$$C_1 = \frac{(1+n)^2}{(1+2n)(2+3n)}, \qquad C_2 = \frac{n^2(3+5n)(1+n)}{(1+2n)^2(2+3n)^2}, \tag{40}$$

$$C_3 = \frac{2+3n}{2(1+n)(1+2n)}, \qquad C_4 = \left(\frac{n}{2+3n}\right)^3, \tag{41}$$

$$C_5 = \frac{n^2(3+4n)}{4(1+2n)^2(1+2n)^2}, \qquad C_6 = \frac{1}{(1+n)(2+n)}. \tag{42}$$

Please see our supplementary material A §3 for the derivation.

5.5 Learning the Conversion Map Θ

The derivation of the Hessian reveals that $\tilde{\mathbf{H}}^{\mathrm{PP}}_{\mathbf{M};\mathrm{S}^{\mathrm{PP}}}$ in (30) is a function of PL only. Hence, the tip of the loss normal $\boldsymbol{q}_{\max}$ forms a (1D) curved trajectory on the unit sphere, though there seemed to be two degrees of freedom (i.e., P and L). Interestingly, this degeneracy is not a problem when matching up the loss normals, as we will see below.

We relate the losses $\mathcal{L}(\tilde{\mathbf{M}}, \mathbf{M}; \mathrm{S})$ and $\mathcal{L}^{\mathrm{PP}}(\tilde{\mathbf{M}}, \mathbf{M}; \mathrm{S}^{\mathrm{PP}})$ instead of relating $\mathbf{H}$ and $\mathbf{H}^{\mathrm{PP}}$ directly, to avoid any error that might occur in the estimation of the Hessian of $\mathcal{L}$ of a DB setup. We start by defining a matching score between $\mathcal{L}$ and $\mathcal{L}^{\mathrm{PP}}$ as follows. Given the material $\mathbf{M}$ and the pair of setups S and S^{PP}, we compute $\mathbf{H}^{\mathrm{PP}}_{\mathbf{M};\mathrm{S}^{\mathrm{PP}}}$ and obtain the loss normal $\boldsymbol{q}^{\mathrm{PP}}_{\max\mathbf{M};\mathrm{S}^{\mathrm{PP}}}$. Then, for $\tilde{\mathbf{M}}$ in the vicinity of $\mathbf{M}$, we define a 'distance' $d_{\mathbf{M};\mathrm{S}^{\mathrm{PP}}}$ to the similarity set as $d_{\mathbf{M};\mathrm{S}^{\mathrm{PP}}}(\tilde{\mathbf{M}}) = |\boldsymbol{q}^{\mathrm{PP}\ \top}_{\max\mathbf{M};\mathrm{S}^{\mathrm{PP}}}(\tilde{\mathbf{M}} - \mathbf{M})|$, measured as the distance to the plane defined by $\boldsymbol{q}^{\mathrm{PP}}_{\max\mathbf{M};\mathrm{S}^{\mathrm{PP}}}$ at $\mathbf{M}$. Then, for a given local region $\Omega_{\mathbf{M}}$ centered at $\mathbf{M}$,

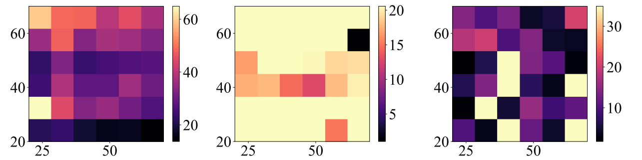

$(24.4, 0.35, 13.7)$ $(17.2, 0.629, 35.0)$ $(13.2, 0.977, 1.21 \times 10^{-6})$

Fig. 9. **Condition numbers of Hessians** computed using the finite difference approximation for different setups (horizontal and vertical axes correspond to width and height of the setup). Please see our supplementary material A §5 for other materials.

we compute the matching score $S_{\mathbf{M};\mathbf{S},\mathbf{S}^{\mathrm{PP}}}$ as a weighted sum of the DB loss values, weighing values higher at $\tilde{\mathbf{M}}$ near the similarity set:

$$S_{\mathbf{M};\mathbf{S},\mathbf{S}^{\mathrm{PP}}} = \frac{\sum_{\tilde{\mathbf{M}}\in\Omega_{\mathbf{M}}} \exp(-d_{\mathbf{M};\mathbf{S}^{\mathrm{PP}}}(\tilde{\mathbf{M}})/d_0)\mathcal{L}(\tilde{\mathbf{M}},\mathbf{M};\mathbf{S})}{\sum_{\tilde{\mathbf{M}}\in\Omega_{\mathbf{M}}} \exp(-d_{\mathbf{M};\mathbf{S}^{\mathrm{PP}}}(\tilde{\mathbf{M}})/d_0)}, \tag{43}$$

where we used $d_0 = 0.025$. A lower value of the score indicates a better match-up.

We find the closest $\mathbf{S}^{\mathrm{PP}}$ for $\mathbf{M}$ and $\mathbf{S}$ using a grid search (i.e., a 1D search done for PL). As we show in Figure 6 (see our supplementary material A §6 for the full results), the match up in the orientations of the similarity sets is pretty good. Then, we learn the function $\mathbf{S}^{\mathrm{PP}} = \Theta(\mathbf{M},\mathbf{S})$ using the searched results for the 200 pairs of $\mathbf{M}$ and $\mathbf{S}$ corresponding to the 200 landscapes $\mathfrak{L}$, and additionally chosen 850 pairs of $\mathbf{M}$ and $\mathbf{S}$ to improve the conversion map near the boundary of the material space $\mathfrak{M}$. As the model for Θ, we found that a second order polynomial of w, h, η, n, σ_{Y}, w^{-1}, h^{-1}, η^{-1}, n^{-1}, and $\sigma_{\mathrm{Y}}{}^{-1}$ was sufficient; it was important to include the reciprocal terms w^{-1}, etc., and the second order helps to account for products, such as w/h. We show the detailed expression of the learned result in our supplementary material A §6.

6 VIRHEOMETRY USING THE SIMILARITY STRUCTURE

We choose the initial setup uniformly randomly from $\mathbb{S}_{\mathrm{exp}}$. In numerical optimization, the efficiency of the optimization is usually determined by the condition number of the problem (in our case, the ratio between the smallest and largest eigenvalues of the Hessian of the loss function). The finite difference approximation of the Hessians (Figure 9) provides us an insight that a lower condition number can happen anywhere in the setup space, meaning that any setup within the range can be a good initial setup (for a particular material). In addition, we suppose the user has no prior knowledge on the material parameters. Thus, we decided to use this random sampling approach for the initial setup.

Once we obtain an estimate $\hat{\mathbf{M}}$ on the material parameters using CMA-ES, we find the new setup $\mathbf{S}_{\mathrm{new}}$ such that its loss normal (computed by Algorithm 2) is 'most perpendicular' to the previously chosen setups. For the loss normals $\boldsymbol{q}_{\max i}$ of the previous setups and that $\boldsymbol{q}_{\max_{\mathrm{new}}}$ of the new setup, we define the perpendicularity score $S_{\mathrm{p}} = \sqrt{\sum_i (\boldsymbol{q}_{\max i} \cdot \boldsymbol{q}_{\max_{\mathrm{new}}})^2}$, and find the new setup with the smallest perpendicularity score. We measure this perpendicularity (i.e., $\boldsymbol{q}_{\max i} \cdot \boldsymbol{q}_{\max_{\mathrm{new}}}$) in the *normalized* material space. For the second setup for instance, the new setup is the one that minimizes the absolute cosine between the two loss normals.

To run CMA-ES, there are three parameters to be determined: 1) the initial variance parameter Σ, 2) the population count n_{p} per each search, and 3) the number of search generations n_{s}. For 1), we decrease the variance parameter as the number of setups increases: for k-th setup ($k \geq 1$), we use $(2/3)^{k-1}$. For 2), we use the formula (6) in the work of Hansen and Kern [2004] and set $n_{\mathrm{p}} = 7$. For 3), we set n_{s} to 100, which would result in $n_{\mathrm{p}} \times n_{\mathrm{s}} \times N$ simulations for the N-th setup (700 and 1,400 simulations for the first and second setups).

For the initial guess $\mathbf{M}_{\mathrm{Init}}$ of the material parameter used during the optimization with the first setup we take the center point of the material parameter space. We configured MPM using uGIMP [Bardenhagen and Kober 2004] and APIC [Jiang et al. 2015], and used Taichi [Hu et al. 2019] for implementation. Running CMA-ES and MPM simulations on an NVIDIA A 100 GPU, it takes about 8 and 16 hours to complete the optimizations for the first and second setups. Our code is available online at https://github.com/AGU-Graphics/ViRheometry.git.

The manual work done in the experiments consists of 1) setting up the dam break configuration, 2) taking video footage, and 3) using the fSpy software [Stuffmatic 2018] for calibration. These in total result in about 1 hour per experiment. Hence, the total manual workload per material is about 2 to 3 hours, which is considerably shorter than manually tweaking the parameters to match the simulations with captured footage (it took weeks for reproducing foams in the work of Yue et al. [2015]).

7 RESULTS

7.1 Validation via 3D Emulations

We chose 6 materials from the material space $\mathfrak{M}$ (we show their distribution in our supplementary material A §8), and used our method to estimate their material parameters. In this assessment, we used 3D MPM simulations to *emulate* the captured frames, instead of performing real experiments. Note that because we are using simulations in place of real experiments, the optimization is *noiseless* in the emulations (hence better results can be expected than using real experiments). We define the relative error $E_{\mathrm{rel}}(\mathbf{M}^\star,\mathbf{M})$ between material parameters $\mathbf{M}^\star = (\eta^\star, n^\star, \sigma_{\mathrm{Y}}{}^\star)$ and $\mathbf{M} = (\eta, n, \sigma_{\mathrm{Y}})$ as

$$E_{\mathrm{rel}}(\mathbf{M}^\star,\mathbf{M}) = \sqrt{\left(\frac{\eta-\eta^\star}{\eta_{\max}-\eta_{\min}}\right)^2 + \left(\frac{n-n^\star}{n_{\max}-n_{\min}}\right)^2 + \left(\frac{\sigma_{\mathrm{Y}}-\sigma_{\mathrm{Y}}{}^\star}{\sigma_{\mathrm{Y}\max}-\sigma_{\mathrm{Y}\min}}\right)^2}, \tag{44}$$

where $\eta_{\min}$, $\eta_{\max}$, $n_{\min}$, $n_{\max}$, $\sigma_{\mathrm{Y}\min}$, and $\sigma_{\mathrm{Y}\max}$ are the bounds of the material space $\mathfrak{M}$.

We first compare the performance using only a single setup and that using two setups. In this comparison, we consider $E_{\mathrm{rel}}(\mathbf{M}^\star,\mathbf{M}) \leq 0.1$ as good enough. The optimization using two setups will run in total 2,100 simulations (700 for the first setup and 700×2 during the second setup). Thus, we also run the optimization using only a single setup up to 2,100 simulation count for fairness (e.g., Figure 10 (a)), but we terminate at 700 simulation count if the relative error of the estimation was already good enough (i.e., $E_{\mathrm{rel}}(\mathbf{M}^\star,\mathbf{M}) \leq 0.1$) or it tends to stuck (which we judge by the variance of the CMA-ES population), e.g., Figure 10 (b). The single setup and the first setup

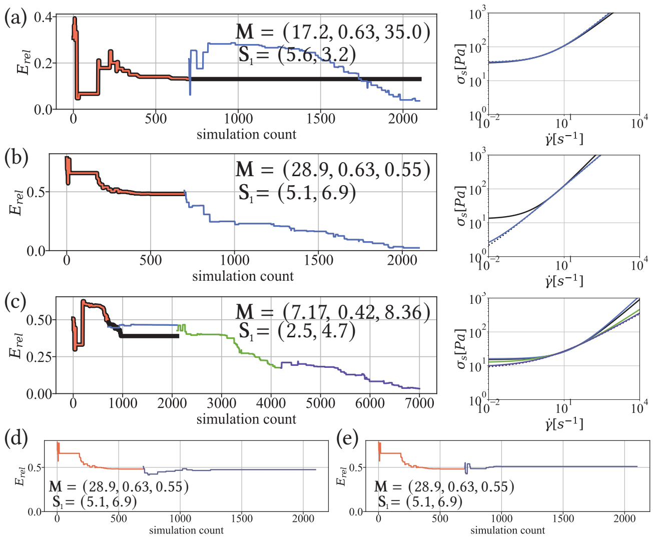

Fig. 10. **Relative errors vs. simulation count, and flow curves.** In (a) to (e), black lines correspond to the single setup cases, and orange, blue, green and purple lines correspond to the first (identical to the single setup case up to 700 simulation count), second, third and fourth setups in the multiple setup cases. In (a) to (c) right, we are showing the flow curves corresponding to the last simulation count of the black, blue, green and purple lines in the relative error plots (in the left), as well as the ground truth flow curves (shown as dotted lines).

are identical for fairness. For each of the materials, we performed the tests 5 times (each starting from a randomly selected first setup). The full results can be found in the supplementary material A §8.

For in total the $6 \times 5 = 30$ cases, 11 cases were already good enough using only the single setup. For these 11 cases, continuing using a second setup did not hurt the results; they also resulted in $E_{\mathrm{rel}}(\mathbf{M}^{\star}, \mathbf{M}) \leq 0.1$. For the remaining 19 cases, using the two setups resulted in 9 cases reached $E_{\mathrm{rel}}(\mathbf{M}^{\star}, \mathbf{M}) \leq 0.1$ (e.g., Figure 10(a)), and the performance of the remaining 10 cases were comparable to or better than using the single setup (e.g., Figure 10(c)). We also continued using a third setup for these 10 cases, which resulted in further improvements (e.g., Figure 10(c)), with 6 of them reached $E_{\mathrm{rel}}(\mathbf{M}^{\star}, \mathbf{M}) \leq 0.1$. Using a fourth setup, all the remaining 4 cases reached $E_{\mathrm{rel}}(\mathbf{M}^{\star}, \mathbf{M}) \leq 0.1$ (e.g., Figure 10 (c)).

We also compared the results in terms of the flow curves. As in Figure 10, it is interesting to note that even though the relative error might seem large, the flow curves for the range[16] of shear rate of $10^{-2} \leq \dot{\gamma} \leq 10^{4}$ sometimes show nice agreement with those of the ground truth material parameters, with the differences mostly seen in the extremely low and high shear rate regimes (usually the power-law index n is easier to determine than the yield stress σ_{Y} and the consistency parameter η; in the log-log plot of the flow curves, n roughly corresponds to the 'slope' of the curves, while σ_{Y} and η have higher impact on the low and high shear rate regimes, respectively). We believe this is because the observations mainly provide information on the intermediate range of the shear rate.

In addition, we tested selecting a second setup with a loss normal similar (i.e., minimum perpendicularity as opposed to maximum perpendicularity in our method) to the first setup (but distant from the first setup) (compare Figure 10 (b) and (d)), as well as using the frames from a different view in place of the second setup (compare Figure 10(b) and (e)). These usually resulted in inferior performance compared to ours (as expected because the second one chosen this way would have a similar similarity set as the first setup).

7.2 Validation via 3D Real-World Experiments

We built our device for the dam-break experiments using only off-the-shelf components. For the walls, we used clear acrylic plates so that we can see the inside. The floor is made of opaque acrylic plate. These plates were cut by a laser cutting machine and glued together. These operations can be easily done at a nearby DIY shop. As in Figure 1, the width w can be tuned by adjusting the position of the back panel. We pour the specimen of interest until the height reaches the specified value h. To start the experiment, we instantly remove the front panel upward. Due to the manual operation, the removal of the front panel takes about 0.02 to 0.03 seconds. For video shooting, we used a mobile phone with a slo-mo mode to obtain a 240 fps video. As the start of the flow, we choose the frame where the bottom tip of the front panel is closest to $\frac{h}{2}$. Starting from that frame, a total of 1/3 seconds (8 frames at 24 fps) is used for optimization. By limiting to this short time window representing the beginning of the flow, the spread of the tip of the specimen is limited and the hope is that the result is less affected by the surface tension. We then extract the silhouettes from the video using the automation functionality available in Adobe Photoshop. The surface mesh of the simulated material is reconstructed using a marching cubes method by Lewiner et al. [2003] and then smoothed using a method by Bhattacharya et al. [2015], which is then rendered with the camera pose calibrated via fSpy [Stuffmatic 2018].

For six materials, moisturizing milk, Japanese pork cutlet sauce (Tonkatsu sauce), Japanese thickened Worcestershire sauce (Chuno sauce), Japanese cabbage pancake sauce (Okonomi sauce), lotion, and sweet bean paste (Tian Mian Jiang), we used a rotational rheometer (Anton-Paar Modular Compact Rheometer MCR 92) with a parallel plate to measure their flow curves plotted as dotted lines in Figure 13. During the measurement, we experienced 5% to 10% deviation in terms of the effective viscosity (hence also the resulting shear stress) per different measurements for the same material. Note that the rheometer makes use of accurately measured kinematic data of the stress and strain rate pairs, whereas ours use no such kinematic data during estimation; just image sequences. We believe our method is doing a good job in matching up the flow curves. We show all the captured and simulated frames in our supplementary material B. For the sweet bean paste, the estimation using a single setup already provided nice agreement, and the introduction of the second setup provided a comparable result. For the moisturizing milk, Japanese pork cutlet sauce, and Japanese thickened Worcestershire sauce, the use of the second setup much improved the estimation, especially for the low to moderate range of shear

[16] Note that the range of $10^{-2} \leq \dot{\gamma} \leq 10^{4}$ is much larger than that ($10^{0} \leq \dot{\gamma} \leq 10^{2}$) can be reliably measured by our rheometer.

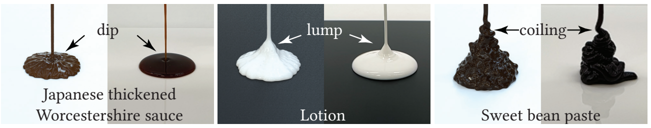

Fig. 11. **Comparison between simulated (left) and captured (right) examples.**

rate (10^0 to 10^1). Note that investigating the differences (shown in supplementary material B) between the captured footage and simulated results for the first setup, we see that the match up is already in a good agreement, and it is the second setup providing additional information for further pinning down the material parameters. We list the estimated material parameters as well as the setups being used in Table 1.

In hindsight, it seems setups near the four corners, (w, h) = (20 mm, 20 mm), (20 mm, 70 mm), (70 mm, 20 mm), (70 mm, 70 mm), help to discern the material parameters. This insight is found as a result of using our technique. Nevertheless, we recommend using our technique to determine the additional setups rather than predetermining additional setups via the corner setups, because 1) the computation cost for finding a new setup is almost negligible compared to other tasks (performing experiments and running optimizations), 2) whether the large (resp. small) geometry, 70 mm (resp. 20 mm), works would be material dependent; the flow can be too fast (resp. slow or even no flow) for certain materials, and 3) using all the four corner setups would require a much longer estimation time, as opposed to our method where two setups are generally sufficient (Figure 13).

In Figure 11, we show a side-by-side comparison between simulated and captured examples using Japanese thickened Worcestershire sauce, lotion, and sweet bean paste for a nozzle-drop scenario. Note that our simulation does not account for the surface tension, hence the surfaces are bumpy. In addition, due to manual injection, the injection speed is not constant; rather, there is up to 20% deviation in the speed over time, which is not accounted for in the simulation. Nevertheless, the comparison indicates that the non-Newtonian viscosity estimated using our ViRheometry technique is able to reproduce a couple of interesting effects. With relatively low effective viscosity, Japanese thickened Worcestershire sauce forms a dip near the location of impact. Lotion, having higher effective viscosity, exhibits wave patterns due to the repetition of stacking (forming a 'lump') and flowing (like 'avalanches'). Having a much higher relative viscosity with sweet bean paste, we observe the coiling behavior. The differences in the flowing behaviors are nicely captured using our simulation.

7.3 Application to materials with inclusions

There are various scenarios the measurements via a rheometer may fail. Even when the inclusions fit in the narrow gap, the measurement may result in a discontinuous or a noisy flow curve, if clogging or non-uniform flows happen in the gap. In addition to that, even when the measured flow curve is smooth, it can be unreliable if the moisture in the material separates and the rest of the material slips over the moisture. We observed that our mustard was this case. The measurement suggests that the flow curve of the mustard is very close to the moisturizing milk, which is not true from the observations of their flowing behaviors. With our method, we successfully identify a much higher effective viscosity, agreeing with the observation.

Table 1. **Experiment settings and estimated material parameters.**

Material	Setup ♯1		Setup ♯2		Estimated parameters		
	w	h	w	h	η	n	σ_Y
Moisturizing milk	2.9	5.9	3.2	2.0	1.27	0.87	14.75
Japanese pork cutlet sauce	6.0	5.8	3.2	2.0	4.02	0.55	1.60
Japanese thickened Worcestershire sauce	2.1	4.0	3.0	2.0	0.55	0.81	1.95
Japanese cabbage pancake sauce	4.2	3.8	2.9	2.0	2.62	0.76	11.58
Lotion	5.1	2.5	7.0	7.0	9.76	0.42	1.46
Sweet bean paste	4.8	4.1	2.1	2.0	10.85	0.75	33.46
Mustard	3.3	6.6	2.3	2.0	4.94	0.85	27.65
Thousand island dressing	3.3	3.6	2.9	2.0	1.49	0.82	13.48
Cobb salad dressing	5.5	4.7	2.9	2.0	1.08	0.87	5.67
Sesame dressing	4.0	4.2	2.9	2.0	0.49	1.00	1.93
Pomodoro sauce	3.2	2.1	7.0	7.0	4.28	0.46	16.98
Carbonara sauce	6.4	3.7	2.5	2.0	7.29	1.00	1.52
Congee	6.4	5.7	2.1	2.0	18.17	0.50	22.90

For materials with inclusions, we used our method to estimate their parameters listed in Table 1. Then, for 1) thousand island dressing, 2) Cobb salad dressing, 3) sesame dressing, 4) Pomodoro sauce, and 5) congee, we simulated animation sequences (Figure 12 and supplementary video) using the estimated parameters. These materials are simulated using the material point method as homogeneous continua. After the simulations, a fraction of the material points are selected as inclusions with random initial orientations, then we track the orientations of these inclusions (using the rotation part of the polar decomposition of the velocity gradient for updating the orientations), and instanced them with the inclusion geometries during rendering. The tweaking of the optical parameters and modeling of the inclusions are out of the scope of this paper and are left for future work. The impression of the flows of these materials agrees with our daily experience quite nicely.

8 CONCLUSIONS, LIMITATIONS AND FUTURE WORK

We have presented a method for estimating the Herschel–Bulkley parameters of various fluid-like materials in our daily life. By matching the flow rule to the scenario assumed in a rotational rheometer, we were able to reproduce nicely matched simulations. By making use of multiple setups, presented using an analysis based on the similarity relation, we were able to improve the estimations. We believe this similarity relation is also useful for machine learning based approaches to design their setups and to evaluate the estimated errors. The parameters obtained by our method is ready for making animations without the need for tweaking the material parameters, which dramatically reduce the manual workload necessary for making an animation.

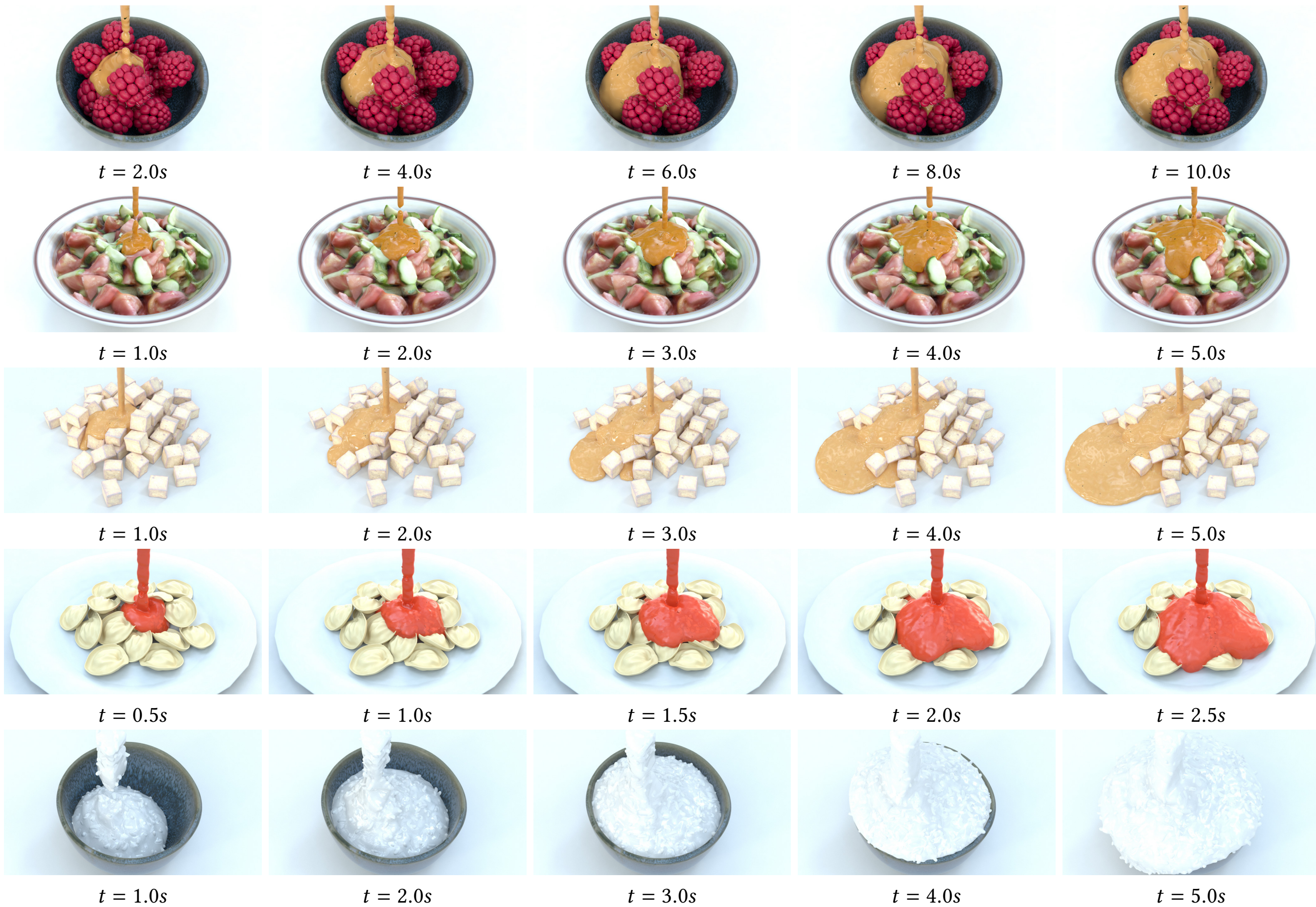

Fig. 12. **Animated results** simulated using material parameters estimated by our method. The materials from top to bottom are thousand island dressing, Cobb salad dressing, sesame dressing, Pomodoro sauce, and congee.

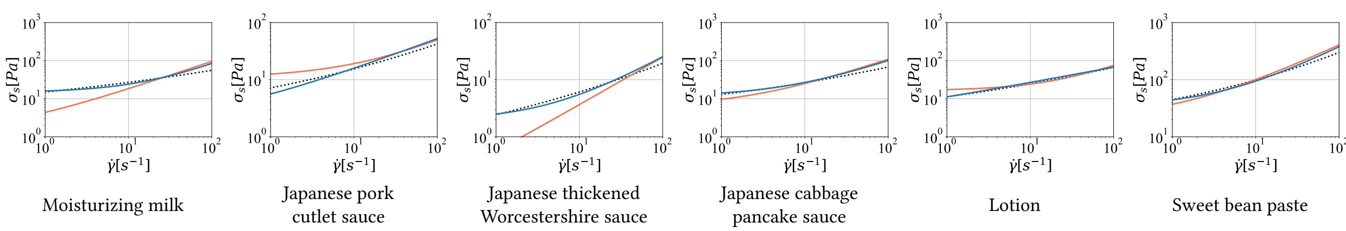

Fig. 13. **Comparison between flow curves.** Dotted: measured by a rotational rheometer. Orange: estimated by using a single setup. Blue: estimated by using two setups.

There are several limitations in our work. First, our method could be inaccurate for thin materials that spread quickly after loading. Such a material may need the handling of the surface tension as well as accurate and rapid motion for opening the front panel. Second, it would be hard to estimate the parameters for materials that flow little. The range of the width and height of the setup implicitly defines a range of shear rate for which the estimation is reliable (which we believe covers the low to moderate shear rate range). It would be an interesting future work to investigate this range quantitatively. Third, although using multiple setups provided comparable or better results than using only a single setup in general, there is no guarantee that this is always the case.

For other future work, it would be beneficial to design an experiment device to automate the setting of the dimensions, the opening of the front panels, and the performance of the calibration. This would further reduce the required manual workload. It would be also interesting to extend our work for elasticity (e.g., for capturing the wiggling motion of a continuum foam), thixotropy, and other constitutive relations, as well as to validate our work for shear thickening materials. The incorporation of NeRF [Mildenhall et al. 2020] or differentiable approaches would be a viable future work (e.g., for handling general flows in the wild, possibly without even using an experiment device). Our insights would be important for their designs. A differentiable approach might be also viable for estimating the Hessians.

ACKNOWLEDGEMENTS

We thank the anonymous reviewers for their insightful suggestions and discussions. We thank Yuxiang Xiong for helping us with the simulations. This work was supported in part by a grant from JST FOREST Program, JPMJFR206R, Japan, a JSPS Grant-in-Aid for Scientific Research on Innovative Areas 18H05001, Japan, a JSPS Grant-in-Aid for Scientific Research (A) 18H04106, Japan, a JSPS Grant-in-Aid for Scientific Research (B) 21H03448, Japan, a JSPS Grant-in-Aid for Challenging Research (Exploratory) 20K21796, Japan, grants from National Natural Science Foundation of China 12174390 and 12150610463, China, and a grant from Wenzhou Institute, University of Chinese Academy of Sciences WIUCASQD2020002, China.

REFERENCES

Faisal As'ad, Philip Avery, and Charbel Farhat. 2022. A mechanics-informed artificial neural network approach in data-driven constitutive modeling. *Internat. J. Numer. Methods Engrg.* 123, 12 (2022), 2738–2759. https://doi.org/10.1002/nme.6957

Scott G. Bardenhagen and Edward M. Kober. 2004. The generalized interpolation material point method. *CMES: Computer Modeling in Engineering and Sciences* 5, 6 (2004), 477–495.

Howard A. Barnes. 2000. *A Handbook of Elementary Rheology.* Institute of Non-Newtonian Fluid Mechanics, University of Wales.

Howard A. Barnes, John Fletcher Hutton, and Kenneth Walters. 1989. *An Introduction to Rheology.* Elsevier Science.

Elena Bayod, Ene Pilman Willers, and Eva Tornberg. 2008. Rheological and structural characterization of tomato paste and its influence on the quality of ketchup. *LWT - Food Science and Technology* 41, 7 (2008), 1289–1300.

Kiran S. Bhat, Steven M. Seitz, and Jovan Popovic. 2002. Computing the physical parameters of rigid-body motion from video. In *Proceedings of the 7th European Conference on Computer Vision-Part I (ECCV '02).* Springer-Verlag, Berlin, Heidelberg, 551–565.

Haimasree Bhattacharya, Yue Gao, and Adam W. Bargteil. 2015. A level-set method for skinning animated particle data. *IEEE Transactions on Visualization and Computer Graphics* 21, 3 (2015), 315–327. https://doi.org/10.1109/TVCG.2014.2362546

Bernd Bickel, Moritz Bächer, Miguel A. Otaduy, Wojciech Matusik, Hanspeter Pfister, and Markus Gross. 2009. Capture and modeling of non-linear heterogeneous soft tissue. *ACM Trans. Graph.* 28, 3, Article 89 (2009), 9 pages. https://doi.org/10.1145/1531326.1531395

Y.J. Choi, K.L. Mccarthy, and M.J. Mccarthy. 2002. Tomographic techniques for measuring fluid flow properties. *Journal of Food Science* 67, 7 (2002), 2718–2724. https://doi.org/10.1111/j.1365-2621.2002.tb08804.x

Maurice M. A. Couette. 1890. Études sur le frottement des liquides. *Ann. Chim. Phys.* Ser. 6, 21 (1890), 433–510.

Philippe Coussot and Jean-Michel Piau. 1995. A large-scale field coaxial cylinder rheometer for the study of the rheology of natural coarse suspensions. *Journal of Rheology* 39, 1 (1995), 105–124. https://doi.org/10.1122/1.550693

Hulya Dogan and Jozef L. Kokini. 2006. Rheological properties of foods. In *Handbook of Food Engineering*, Dennis R. Heldman and Daryl B. Lund (Eds.). CRC Press, 1–124.

D. Eolkin. 1957. The plastometer - A new development in continuous recording and controlling consistometer. *Food Technology* 11 (1957), 253–257.

Yun (Raymond) Fei, Christopher Batty, Eitan Grinspun, and Changxi Zheng. 2019. A multi-scale model for coupling strands with shear-dependent liquid. *ACM Trans. Graph.* 38, 6, Article 190 (2019), 20 pages. https://doi.org/10.1145/3355089.3356532

Gotthilf Heinrich Ludwig Hagen. 1839. Ueber die Bewegung des Wassers in engen cylindrischen Röhren. *Annalen der Physik* 122, 3 (1839), 423–442. https://doi.org/10.1002/andp.18391220304

Nikolaus Hansen and Stefan Kern. 2004. Evaluating the CMA evolution strategy on multimodal test functions. In *Proceedings of Parallel Problem Solving from Nature 2004 (PPSN VIII).* Springer, Berlin, Heidelberg, 282–291. https://doi.org/10.1007/978-3-540-30217-9_29

Gert Heirman, Lucie Vandewalle, Dionys Van Gemert, and O. Wallevik. 2008. Integration approach of the Couette inverse problem of powder-type self-compacting concrete in a wide-gap concentric cylinder rheometer. *Journal of Non-Newtonian Fluid Mechanics* 150, 2 (2008), 93–103.

Winslow H. Herschel and Ronald Bulkley. 1926. Konsistenzmessungen von Gummi-Benzollösungen. *Kolloid-Zeitschrift & Zeitschrift für Polymere* 39, 4 (1926), 291–300.

Yuanming Hu, Tzu-Mao Li, Luke Anderson, Jonathan Ragan-Kelley, and Frédo Durand. 2019. Taichi: A language for high-performance computation on spatially sparse data structures. *ACM Trans. Graph.* 38, 6, Article 201 (2019), 16 pages. https://doi.org/10.1145/3355089.3356506

Daniel Z. Huang, Kailai Xu, Charbel Farhat, and Eric Darve. 2020. Learning constitutive relations from indirect observations using deep neural networks. *J. Comput. Phys.* 416 (2020), 109491. https://doi.org/10.1016/j.jcp.2020.109491

Kyu Hyun, Manfred Wilhelm, Christopher O. Klein, Kwang Soo Cho, Jung Gun Nam, Kyung Hyun Ahn, Seung Jong Lee, Randy H. Ewoldt, and Gareth H. McKinley. 2011. A review of nonlinear oscillatory shear tests: Analysis and application of large amplitude oscillatory shear (LAOS). *Progress in Polymer Science* 36, 12 (2011), 1697–1753. https://doi.org/10.1016/j.progpolymsci.2011.02.002

Chenfanfu Jiang, Craig Schroeder, Andrew Selle, Joseph Teran, and Alexey Stomakhin. 2015. The affine particle-in-cell method. *ACM Trans. Graph. (Proc. of SIGGRAPH 2015)* 34, 4, Article 51 (2015), 10 pages. https://doi.org/10.1145/2766996

Arnd Koeppe, Franz Bamer, Michael Selzer, Britta Nestler, and Bernd Markert. 2022. Explainable artificial intelligence for mechanics: Physics-explaining neural networks for constitutive models. *Frontiers in Materials* 8 (2022). https://doi.org/10.3389/fmats.2021.824958

Ronald G. Larson. 1998. *The Structure and Rheology of Complex Fluids.* Oxford university press.

Thomas Lewiner, Hélio Lopes, Antônio Wilson Vieira, and Geovan Tavares. 2003. Efficient implementation of marching cubes cases with topological guarantees. *Journal of Graphics Tools* 8, 2 (2003), 1–15. https://doi.org/10.1080/10867651.2003.10487582

Xuan Li, Yadi Cao, Minchen Li, Yin Yang, Craig Schroeder, and Chenfanfu Jiang. 2022. PlasticityNet: Learning to simulate metal, sand, and snow for optimization time integration. In *Advances in Neural Information Processing Systems.* https://openreview.net/forum?id=_WqHmwoE7Ud

Felipe R. Loyola, Waldyr de Lima e Silva, Luiz G.C. Campos, and Christian J.L. Hermes. 2018. Rheometric assessment and numerical simulation of steady-state and periodic flows of fabric-water mixtures in household top-load washing machines. *Chemical Engineering Research and Design* 137 (2018), 273–290. https://doi.org/10.1016/j.cherd.2018.07.012

Pingchuan Ma, Peter Yichen Chen, Bolei Deng, Joshua B Tenenbaum, Tao Du, Chuang Gan, and Wojciech Matusik. 2023. Learning neural constitutive laws from motion observations for generalizable PDE dynamics. In *International Conference on Machine Learning (ICML 2023).* PMLR. arXiv:https://arxiv.org/pdf/2304.14369

Geraldo de F. Maciel, Hamilton Kiryu dos Santos, and Fabiana de O. Ferreira. 2009. Rheological analysis of water clay compositions in order to investigate mudflows developing in canals. *Journal of the Brazilian Society of Mechanical Sciences and Engineering* 31, 1 (2009), 64–74. https://doi.org/10.1590/S1678-58782009000100010

Christopher W. Macosko. 1994. *Rheology: Principles, Measurements, and Applications.* Wiley-VCH, Inc.

Elie Magnon and Eric Cayeux. 2021. Precise method to estimate the Herschel–Bulkley parameters from pipe rheometer measurements. *Fluids* 6, 4, Article 157 (2021). https://doi.org/10.3390/fluids6040157

Rolf Mahnken. 2004. Identification of material parameters for constitutive equations. In *Encyclopedia of Computational Mechanics.* John Wiley & Sons, Ltd, Chapter 19, 637–655. https://doi.org/10.1002/0470091355.ecm043

Kathryn L. McCarthy and Michael J. McCarthy. 2009. Relationship between in-line viscosity and Bostwick measurement during ketchup production. *Journal of Food Science* 74, 6 (2009), E291–E297.

Thomas G. Mezger. 2012. *The Rheology Handbook: 4th Edition.* Vincentz Network. https://doi.org/doi:10.1515/9783748600367

Rebecca R. Milczarek and Kathryn L. McCarthy. 2006. Relationship between the Bostwick measurement and fluid properties. *Journal of Texture Studies* 37, 6 (2006), 640–654. https://doi.org/10.1111/j.1745-4603.2006.00075.x

Ben Mildenhall, Pratul P. Srinivasan, Matthew Tancik, Jonathan T. Barron, Ravi Ramamoorthi, and Ren Ng. 2020. NeRF: Representing scenes as neural radiance fields for view synthesis. In *Proceedings of the European Conference on Computer Vision (ECCV).* http://arxiv.org/abs/2003.08934v2

Aron Monszpart, Nils Thuerey, and Niloy J. Mitra. 2016. SMASH: Physics-guided reconstruction of collisions from videos. *ACM Trans. Graph.* 35, 6, Article 199 (2016), 14 pages. https://doi.org/10.1145/2980179.2982421

Melvin Mooney and Roswell H. Ewart. 1934. The conicylindrical viscometer. *Physics* 5, 11 (1934), 350–354. https://doi.org/10.1063/1.1745219
Glen Mullineux. 2008. Non-linear least squares fitting of coefficients in the Herschel–Bulkley model. *Applied Mathematical Modelling* 32, 12 (2008), 2538–2551. https://doi.org/10.1016/j.apm.2007.09.010
J. Krishna Murthy, Miles Macklin, Florian Golemo, Vikram Voleti, Linda Petrini, Martin Weiss, Breandan Considine, Jérôme Parent-Lévesque, Kevin Xie, Kenny Erleben, Liam Paull, Florian Shkurti, Derek Nowrouzezahrai, and Sanja Fidler. 2021. gradSim: Differentiable simulation for system identification and visuomotor control. In *ICLR 2021 posters*. https://openreview.net/forum?id=c_E8kFWfhp0
Kentaro Nagasawa, Takayuki Suzuki, Ryohei Seto, Masato Okada, and Yonghao Yue. 2019. Mixing sauces: A viscosity blending model for shear thinning fluids. *ACM Trans. Graph. (Proc. of SIGGRAPH 2019)* 38, 4, Article 95 (2019), 17 pages. https://doi.org/10.1145/3306346.3322947
Anna Maria Pellegrino and Leonardo Schippa. 2018. A laboratory experience on the effect of grains concentration and coarse sediment on the rheology of natural debris-flows. *Environmental Earth Sciences* 77 (2018), 749:1–13. https://doi.org/10.1007/s12665-018-7934-0
Paolo Perona. 2005. Bostwick degree and rheological properties: An up-to-date viewpoint. *Applied Rheology* 15, 4 (2005), 218–229. https://doi.org/10.1515/arh-2005-0013
Jean Léonard Marie Poiseuille. 1840. Recherches expérimentales sur le mouvement des liquides dans les tubes de très-petit diamètres. *Comptes Rendus Hebdomadaires des Séances de l'Académie des Sciences* 11 (1840), 961–1041.
Abdullah Haroon Rasheed, Victor Romero, Florence Bertails-Descoubes, Stefanie Wuhrer, Jean-Sebastien Franco, and Arnaud Lazarus. 2021. A visual approach to measure cloth-body and cloth-cloth friction. *IEEE Transactions on Pattern Analysis and Machine Intelligence* (2021), 1–1. https://doi.org/10.1109/TPAMI.2021.3097547
D. S. Sankar and Usik Lee. 2016. Influence of slip velocity in Herschel–Bulkley fluid flow between parallel plates - A mathematical study. *Journal of Mechanical Science and Technology* 30, 7 (2016), 3203––3218. https://doi.org/10.1007/s12206-016-0629-0
Yuri Taglieri Sáo, João Batista Pereira, Guilherme Henrique Fiorot, and Geraldo de Freitas Maciel. 2021. Obtaining flow curve for viscoplastic fuids through inclined open-channel apparatus. *Journal of the Brazilian Society of Mechanical Sciences and Engineering* 43 (2021), 278:1–17. https://doi.org/10.1007/s40430-021-02999-2
Saeid Savarmand, Mourad Heniche, Vincent Béchard, François Bertrand, and Pierre J. Carreau. 2007. Analysis of the vane rheometer using 3D finite element simulation. *Journal of Rheology* 51, 2 (2007), 161–177. https://doi.org/10.1122/1.2433936
M. Schatzmann, G. R. Bezzola, H.-E. Minor, E. J. Windhab, and P. Fischer. 2009. Rheometry for large-particulated fluids: Analysis of the ball measuring system and comparison to debris flow rheometry. *Rheologica Acta* 48 (2009), 715–733. https://doi.org/10.1007/s00397-009-0364-x
Juan. C. Simo. 1988. A framework for finite strain elastoplasticity based on maximum plastic dissipation and the multiplicative decomposition: Part I. continuum formulation. *Computer Methods in Applied Mechanics and Engineering* 66, 2 (1988), 199–219.
Juan C. Simo and Thomas J. R. Hughes. 1998. *Computational Inelasticity*. Springer.
Juan C. Simo and Christian Miehe. 1992. Associative coupled thermoplasticity at finite strains: Formulation, numerical analysis and implementation. *Computer Methods in Applied Mechanics and Engineering* 98, 1 (1992), 41–104. https://doi.org/10.1016/0045-7825(92)90170-O
Alexey Stomakhin, Craig Schroeder, Lawrence Chai, Joseph Teran, and Andrew Selle. 2013. A material point method for snow simulation. *ACM Trans. Graph. (Proc. of SIGGRAPH 2013)* 32, 4, Article 102 (2013), 10 pages. https://doi.org/10.1145/2461912.2461948
Stuffmatic. 2018. fSpy: Open source still image camera matching. https://fspy.io/. Accessed: 2023-09-18.
Deborah Sulsky, Zhen Chen, and Howard L. Schreyer. 1994. A particle method for history-dependent materials. *Computer Methods in Applied Mechanics and Engineering* 118, 1 (1994), 179–196.
Deborah Sulsky, Shi-Jian Zhou, and Howard L. Schreyer. 1995. Application of a particle-in-cell method to solid mechanics. *Computer Physics Communications* 87, 1-2 (1995), 236–252.
Tetsuya Takahashi and Ming C. Lin. 2019. Video-guided real-to-virtual parameter transfer for viscous fluids. *ACM Trans. Graph. (Proc. of SIGGRAPH Asia 2019)* 38, 6, Article 237 (2019), 12 pages. https://doi.org/10.1145/3355089.3356551
Clifford Truesdell and Walter Noll. 1965. *The Non-Linear Field Theories of Mechanics*. Springer Berlin, Heidelberg.
Nikolaos N. Vlassis and WaiChing Sun. 2021. Sobolev training of thermodynamic-informed neural networks for interpretable elasto-plasticity models with level set hardening. *Computer Methods in Applied Mechanics and Engineering* 377 (2021), 113695. https://doi.org/10.1016/j.cma.2021.113695
Bin Wang, Yuanmin Deng, Paul Kry, Uri Ascher, Hui Huang, and Baoquan Chen. 2020. Learning elastic constitutive material and damping models. *Computer Graphics Forum* 39, 7 (2020), 81–91. https://doi.org/10.1111/cgf.14128
Bin Wang, Longhua Wu, KangKang Yin, Uri Ascher, Libin Liu, and Hui Huang. 2015. Deformation capture and modeling of soft objects. *ACM Trans. Graph. (Proc. of SIGGRAPH 2015)* 34, 4, Article 94 (2015), 12 pages. https://doi.org/10.1145/2766911
Judith K. Whaley, Catherine Templeton, and Mohammad Anvari. 2019. Rheological testing for semisolid foods: Traditional rheometry. In *Rheology of Semisolid Foods*, Helen S. Joyner (Ed.). Springer International Publishing, 63–96. https://doi.org/10.1007/978-3-030-27134-3_3
Yonghao Yue, Breannan Smith, Christopher Batty, Changxi Zheng, and Eitan Grinspun. 2015. Continuum foam: A material point method for shear-dependent flows. *ACM Trans. Graph.* 34, 5, Article 160 (2015), 20 pages. https://doi.org/10.1145/2751541
Yalan Zhang, Zirui Dong, Mohammad S. Obaidat, and Xiaojuan Ban. 2023. Non-Newtonian fluid simulation and reconstruction from monocular videos. *Simulation Modelling Practice and Theory* 123 (2023), 102688. https://doi.org/10.1016/j.simpat.2022.102688
Shuang Zhao, Ravi Ramamoorthi, and Kavita Bala. 2014. High-order similarity relations in radiative transfer. *ACM Trans. Graph.* 33, 4, Article 104 (2014), 12 pages. https://doi.org/10.1145/2601097.2601104
Haotian Zheng. 2019. Introduction: Measuring rheological properties of foods. In *Rheology of Semisolid Foods*, Helen S. Joyner (Ed.). Springer International Publishing, 3–30. https://doi.org/10.1007/978-3-030-27134-3_1

A PRINCIPLE OF MAXIMUM PLASTIC DISSIPATION

We briefly review the derivation of the flow rule by Simo and Miehe [1992]. Following a Clausius–Plank form [Truesdell and Noll 1965] of the second law (in the push-forwarded configuration), we have the following dissipation inequality (in this paper, we are omitting material hardening/softening for simplicity):

$$\mathcal{D} = \boldsymbol{\tau} : \mathbf{d} - \dot{\psi} \geq 0, \tag{45}$$

where $\mathcal{D}$ is the dissipation rate, $\boldsymbol{\tau} = J\boldsymbol{\sigma}$ is the Kirchhoff stress, $\mathbf{d}$ is the shear rate tensor, and ψ is the stored (or strain) energy density. $\mathbf{d}$ is the symmetric part of the velocity gradient $\mathbf{L} = \nabla \boldsymbol{v}$: $\mathbf{d} = \mathrm{sym}[\mathbf{L}] = \frac{\mathbf{L}+\mathbf{L}^\top}{2}$.

With (9), the time derivative of ψ is given by

$$\dot{\psi} = \frac{\partial \psi}{\partial \mathbf{b}_\mathrm{e}} : \dot{\mathbf{b}}_\mathrm{e} = \frac{\partial \psi}{\partial \mathbf{b}_\mathrm{e}} : \left(\mathbf{L}\mathbf{b}_\mathrm{e} + \mathbf{b}_\mathrm{e}\mathbf{L}^\top + \mathcal{L}_{\boldsymbol{v}}\mathbf{b}_\mathrm{e} \right). \tag{46}$$

Using 1) matrix identities $\mathbf{A} : (\mathbf{BC}) = (\mathbf{AC}^\top) : \mathbf{B}$ and $\mathbf{A} : (\mathbf{BC}) = (\mathbf{B}^\top\mathbf{A}) : \mathbf{C}$, 2) the fact that $\mathbf{b}_\mathrm{e}$, $\frac{\partial \psi}{\partial \mathbf{b}_\mathrm{e}}$ and $\mathcal{L}_{\boldsymbol{v}}\mathbf{b}_\mathrm{e}$ commute with each other, and 3) the fact that $\frac{\partial \psi}{\partial \mathbf{b}_\mathrm{e}}$ and $\mathbf{b}_\mathrm{e}$ are symmetric, we have

$$\dot{\psi} = \frac{\partial \psi}{\partial \mathbf{b}_\mathrm{e}}\mathbf{b}_\mathrm{e} : \left(\mathbf{L} + \mathbf{L}^\top + (\mathcal{L}_{\boldsymbol{v}}\mathbf{b}_\mathrm{e})\mathbf{b}_\mathrm{e}{}^{-1} \right) = 2\frac{\partial \psi}{\partial \mathbf{b}_\mathrm{e}}\mathbf{b}_\mathrm{e} : \left(\mathbf{d} + \frac{1}{2}(\mathcal{L}_{\boldsymbol{v}}\mathbf{b}_\mathrm{e})\mathbf{b}_\mathrm{e}{}^{-1} \right). \tag{47}$$

Substituting into the definition of the dissipation rate, the second law becomes

$$\mathcal{D} = \left(\boldsymbol{\tau} - 2\frac{\partial \psi}{\partial \mathbf{b}_\mathrm{e}}\mathbf{b}_\mathrm{e} \right) : \mathbf{d} + \left(2\frac{\partial \psi}{\partial \mathbf{b}_\mathrm{e}}\mathbf{b}_\mathrm{e} \right) : \left(-\frac{1}{2}(\mathcal{L}_{\boldsymbol{v}}\mathbf{b}_\mathrm{e})\mathbf{b}_\mathrm{e}{}^{-1} \right) \geq 0. \tag{48}$$

Because the above inequality must be satisfied irrespective of the shear rate tensor $\mathbf{d}$, we must have

$$\boldsymbol{\tau} = 2\frac{\partial \psi}{\partial \mathbf{b}_\mathrm{e}}\mathbf{b}_\mathrm{e}, \tag{49}$$

which immediately gives us (10). The second law then becomes

$$\mathcal{D} = \boldsymbol{\tau} : \left(-\frac{1}{2}(\mathcal{L}_{\boldsymbol{v}}\mathbf{b}_\mathrm{e})\mathbf{b}_\mathrm{e}{}^{-1} \right) \geq 0. \tag{50}$$

Simo and Miehe [1992] then introduce the principle of maximum plastic dissipation, stating that for any stress $\tilde{\boldsymbol{\tau}} \in \mathfrak{E}$ within the admissible elastic regime $\mathfrak{E}$ defined by the yield condition, $\boldsymbol{\tau}$ must satisfy

$$(\boldsymbol{\tau} - \tilde{\boldsymbol{\tau}}) : \left(-\frac{1}{2}(\mathcal{L}_{\boldsymbol{v}}\mathbf{b}_\mathrm{e})\mathbf{b}_\mathrm{e}{}^{-1} \right) \geq 0. \tag{51}$$

This implies that the flow $\left(-\frac{1}{2}(\mathcal{L}_{\boldsymbol{v}}\mathbf{b}_\mathrm{e})\mathbf{b}_\mathrm{e}{}^{-1}\right)$ occurs in the direction normal to $\mathfrak{E}$, or in other words, normal to the yield function $\Phi(\boldsymbol{\sigma};\sigma_\mathrm{Y})$. This gives rise to the associative flow rule (11).

B DISCRETE RETURN MAPPING

The treatment of the elasto-viscoplasticity [Simo and Hughes 1998; Yue et al. 2015] at the m-th simulation step consists of an explicit *elastic prediction* step

$$\mathbf{b}_{\mathrm{e,pre}} = \mathbf{b}_{\mathrm{e},m} + \Delta t(\mathbf{L}_m\mathbf{b}_{\mathrm{e},m} + \mathbf{b}_{\mathrm{e},m}\mathbf{L}_m^\top), \tag{52}$$

where Δt is the time step, followed by an implicit *plastic correction* step discretizing (18):

$$\mathbf{b}_{\mathrm{e},m+1} - \mathbf{b}_{\mathrm{e,pre}} = -\Delta t\dot{\gamma}_{\mathrm{HB},m+1}\left(\sqrt{2}\frac{\mathrm{dev}[\boldsymbol{\sigma}_{m+1}]}{\|\,\mathrm{dev}[\boldsymbol{\sigma}_{m+1}]\|_\mathrm{F}}\right)\mathbf{b}_{\mathrm{e},m+1}. \tag{53}$$

As in our supplementary material A §1, (53) can be solved using a Newton method in the eigenspace of $\mathbf{b}_\mathrm{e}$. Computationally, it suffices to introduce an approximation as in Simo [1988], for a more light weight computation. Substituting $\mathbf{b}_\mathrm{e} = \frac{1}{d}\,\mathrm{tr}[\mathbf{b}_\mathrm{e}]\mathbf{I}+\mathrm{dev}[\mathbf{b}_\mathrm{e}]$ into (18), we have

$$\mathcal{L}_{\boldsymbol{v}}\mathbf{b}_\mathrm{e} = -\dot{\gamma}_\mathrm{HB}\left(\sqrt{2}\frac{\mathrm{dev}[\boldsymbol{\sigma}]}{\|\,\mathrm{dev}[\boldsymbol{\sigma}]\|_\mathrm{F}}\right)\left(\frac{1}{d}\,\mathrm{tr}[\mathbf{b}_\mathrm{e}]\mathbf{I} + \mathrm{dev}[\mathbf{b}_\mathrm{e}]\right). \tag{54}$$

For μ sufficiently large, $\mathrm{dev}[\mathbf{b}_\mathrm{e}]$ is close to $\mathbf{O}$, and $\|\,\mathrm{dev}[\mathbf{b}_\mathrm{e}]\|_\mathrm{F} \ll \|\frac{1}{d}\,\mathrm{tr}[\mathbf{b}_\mathrm{e}]\mathbf{I}\|_\mathrm{F}$, so one can omit the second term in the right parentheses and have

$$\mathcal{L}_{\boldsymbol{v}}\mathbf{b}_\mathrm{e} \approx -\dot{\gamma}_\mathrm{HB}\frac{\sqrt{2}}{d}\,\mathrm{tr}[\mathbf{b}_\mathrm{e}]\frac{\mathrm{dev}[\boldsymbol{\sigma}]}{\|\,\mathrm{dev}[\boldsymbol{\sigma}]\|_\mathrm{F}}, \tag{55}$$

resulting in a discrete form

$$\mathbf{b}_{\mathrm{e},m+1} - \mathbf{b}_{\mathrm{e,pre}} \approx -\Delta t\dot{\gamma}_{\mathrm{HB},m+1}\frac{\sqrt{2}}{d}\,\mathrm{tr}[\mathbf{b}_{\mathrm{e},m+1}]\frac{\mathrm{dev}[\boldsymbol{\sigma}_{m+1}]}{\|\,\mathrm{dev}[\boldsymbol{\sigma}_{m+1}]\|_\mathrm{F}}. \tag{56}$$

We can then derive a return mapping similar to Yue et al. [2015] (with slight modification in the coefficients), which amounts to solve the following scalar equation for $\sigma_{\mathrm{s},m+1}$:

$$\sigma_{\mathrm{s},m+1} - \sigma_{\mathrm{s,pre}} = -\frac{\sqrt{2}}{d}\Delta t\frac{\mu}{J}\,\mathrm{tr}[\mathbf{b}_{\mathrm{e,pre}}]\left(\frac{\frac{1}{\sqrt{2}}\sigma_{\mathrm{s},m+1} - \sigma_\mathrm{Y}}{\eta}\right)^{1/n}, \tag{57}$$

via a Newton method. The purple lines produced in Figure 5 is created with this approach, indicating that the accuracy is sufficient enough. We summarize the details in our supplementary material A §1. In our supplementary material A §1, we also discuss the analytical form introduced by Fei et al. [2019].